Adaptive Fractional-Order Resonant Control with Fixed-Time Augmented Extended State Observer for Current Disturbance Attenuation in Electric Propulsion System

Jiaxing Ye, *Graduate Student Member, IEEE*, Mingyi Wang, Shun Cai, Chaoyu Zhang, Pedram Asef, *Senior Member, IEEE*, Sihang Cui, Junchi Li, Jinrui Xie, Zihan Hu, Chengming Zhang and Liyi Li, *Senior Member, IEEE*

***Abstract*—Classical current control strategies in electric propulsion systems often suffer from degraded performance under periodic and aperiodic disturbances. To overcome these limitations, this paper proposes a novel current control framework that combines an adaptive fractional-order resonant controller (AFRC) with a fixed-time augmented extended state observer (FxTAESO), aiming to enhance disturbance rejection and dynamic robustness. Firstly, the proposed AFRC introduces a self-tuning fractional-order operator, which adaptively adjusts in real-time according to load current, harmonic rejection strength, and desired phase margin. This adaptive mechanism enables precise harmonic compensation while ensuring stability and robustness across the varying operating conditions. Subsequently, the FxTAESO incorporates a current integral term as system augmented variable to decouple the coupling effect between current measurement noise and high observer gains. Additionally, by embedding an improved nonlinear fixed-time convergence law, the observer ensures that the estimation error converges to a bounded neighborhood of the equilibrium point within a predetermined time, independent of initial conditions. Finally, experimental validation on a PMSM drive platform demonstrates that the proposed FxTAESO-AFRC scheme achieves superior steady-state accuracy, faster transient response, and stronger disturbance suppression compared to conventional methods.**

***Index Terms*—Augmented extended state observer, adaptive fractional-order, current control, electric propulsion system, fixed-time convergence, permanent magnet synchronous motor.**

I. Introduction

PERMANENT magnet synchronous motors (PMSMs) have emerged as a cornerstone technology in modern electric propulsion architectures due to their high energy conversion efficiency, compact structure, and reduced maintenance demands. These advantageous characteristics have facilitated their extensive deployment in a wide range of transportation electrification platforms, including electric and hybrid-electric aircraft, electric vehicles (EVs), and unmanned aerial and robotic systems [1], [2]. Within PMSM-based propulsion systems, the current control loop forms the innermost feedback path and plays a pivotal role in directly regulating the electromagnetic torque output. Hence, the precision and robustness of current regulation critically affect the dynamic performance, torque fidelity, and overall stability of the electric propulsion systems. However, conventional current controllers often face significant challenges in mitigating adverse effects caused by parameter uncertainties, inverter nonlinearities [3], and external disturbances [4]. These nonlinear disturbances can induce steady-state torque ripples, speed oscillations, and degraded the transient responses, which are especially detrimental to the high-performance electrified transportation applications. Therefore, the development of advanced current loop control strategies, particularly those capable of real-time disturbance rejection and robust performance enhancement, is essential for ensuring reliable and efficient operation of PMSM electric propulsion systems.

Based on the underlying mechanism of uncertainties, the disturbances within the current loop of PMSM drive system can be broadly categorized into two primary subtypes [5]. The first subcategory encompasses aperiodic ones. To attenuate these disturbances, a wide range of advanced control theories and strategies have been developed over recent years to enhance the current performance of PMSM [6]-[10]. The approach outlined in [6] demonstrates capability to dynamically adapt to the disturbance based on the actual system. However, the developed technique remains to be a model-based control strategy, heavily relying on high precision of the prior model information. A composite extended Kalman filter (EKF) control strategy was introduced for disturbance estimation in [7]. As EKF operates as a variable gain observer, it provides effective observation performance. While it is computationally overloaded and presents challenge to tune control parameters. This makes its application particularly difficult in high-performance scenarios with short control cycle. Ref. [8] achieves precise current regulation by introducing a stator current self-adjustment model using model predictive control (MPC). Whereas classic MPC faces challenges, including high complexity of optimization calculation and sensitivity to model parameters. A sliding mode observer (SMO) based on adaptive reaching law was proposed in [9]. Although the chattering problem is mitigated, there are still significant current ripples and large overshoots due to parameters mismatch. Recently, extended state observer (ESO) has gained widespread research and adoption in PMSM drive because of its simple structure, ease of parameters tuning, and less dependency on the system model information [10]. However, the observation error of state variables in classic ESO can only converge asymptotically. This will have certain disturbances' estimation errors for motor systems with fast control cycles and

This work was supported in part by the National Natural Science Foundation of China under Grant 52477039, Grant 52450227, and Grant 52421004; in part by the China Postdoctoral Science Foundation under Grant GZC20252692; and in part by the China Scholarship Council under Grant 202406120161. *(Corresponding author: Mingyi Wang).*

Jiaxing Ye, Sihang Cui, Junchi Li, Jinrui Xie, Zihan Hu, Chengming Zhang and Liyi Li are with the Department of Electrical Engineering, Harbin Institute of Technology, Harbin, 150001, China. (e-mail: yejiaxing@stu.hit.edu.cn; 21b906034@stu.hit.edu.cn; lijunchi@stu.hit.edu.cn; 24B906014@stu.hit.edu.cn; 24S106230@stu.hit.edu.cn; cmzhang@hit.edu.cn; liliyi@hit.edu.cn).

Mingyi Wang is with the Department of Electrical Engineering, Harbin Institute of Technology, Harbin 150001, China, and also with Suzhou Research Institute of HIT, Suzhou 215104, China. (email: wangmingyi@hit.edu.cn).

Shun Cai is with the College of Electrical Engineering, Zhejiang University, Hangzhou 310027, China. (e-mail: caishun@zju.edu.cn).

Chaoyu Zhang is with the School of Robotics and Advanced Manufacture, Harbin Institute of Technology, Shenzhen 518052, China (email: zhangchaoyu@hit.edu.cn).

Pedram Asef is with the Department of Mechanical Engineering, University College London, London E20 2AE, United Kingdom. (email: Pedram.asef@ucl.ac.uk).

high real-time requirements, which in turn affects the high-performance current control of PMSMs. Also, the coupling characteristic between the current sampling noise and high observer gain is also a major point of consideration. Therefore, it is important to develop an method for ESO to tackle these undesired deficiencies.

The second subcategory of current disturbances is periodic ones. However, due to the limitations of bandwidth and other factors, classic ESO struggles to effectively predict periodic disturbances. The conventional observer focuses more on the accurate observation of direct-current (DC) and slow time-varying signals. Hence, it is imperative to develop composite control strategies to enhance the rejection abilities of periodic harmonics. Iterative learning control (ILC) has been extensively used in repeated motion control and periodic disturbances suppression in PMSM drives [11], but it requires large amounts of data storage and is dependent on the specific initial state. In [12], repetitive control was utilized to process the periodic reference signals. However, the algorithm has a long convergence time and is challenging to implement when the frequency of disturbances is variable. For these reasons, resonant controller has received much attention recently in both academia and industrial communities for their structural flexibility and superior computational efficiency. In [13], the method of introducing resonant components to the PI controller was proposed to achieve smooth speed control and to avoid speed overshoots during transients by mode switching. Ref. [14] achieved sinusoidal disturbances tracking with fast time-varying characteristics in grid-connected inverter using a generalized integrator-based ESO. Similarly, the Ref. [15] achieved smooth speed control by embedding an adaptive generalized integrator in the ESO. However, none of the above schemes consider the constraints between resonant gain and system stability. Moreover, system stability may be degraded due to the delay property of the controlled plant. Therefore, in [16], a vector resonant control (VRC) was developed to remove the phase delay by introducing the controlled plant information. Unfortunately, the amplitude-phase characteristics as well as the immunity of VRC are compromised when the system model parameters are mismatched.

In the existing literatures, recent advances related to fixed-time and noise-tolerant ESOs have been further proposed to improve systems' convergent speed and anti-disturbance performance. Ref. [17] designs a cascaded ESO combined with sliding mode control (SMC) to suppress noise and reduce chattering via disturbance-based switching gain adjustment. Ref. [18] employs a cascaded finite-time SMO with terminal SMC to achieve fast convergence and strong noise rejection for underactuated systems. Ref. [19] develops a fixed-time SMC scheme with a cascaded SMO ensuring convergence independent of initial conditions and low sensitivity to noise. Ref. [20] integrates a fixed-time ESO with an adaptive integral SMC to realize fixed-time stability while effectively mitigating chattering and measurement noise. In the field of motor and precision motion control system, it has introduced diverse advanced control schemes to improve dynamic performance and system robustness. An improved deadbeat predictive current control (DPCC) incorporating a repetitive control-based disturbance correction observer enhances steady-state accuracy and harmonic rejection for PMSM current loop [21]. A model-free finite control set MPC based on an ultra-local model reduces model dependence while increasing computational burden and tuning sensitivity [22]. For robust control, a variable-structure active disturbance rejection control (ADRC) with interconnected ESOs provides strong disturbance rejection and noise suppression [23]. Likewise, a composite super-twisting SMC with a novel disturbance observer achieves high robustness and reduced chattering, yet depends heavily on precise observer calibration [24]. Adaptive and learning-based approaches have been employed to enhance tracking under uncertainty. Ref. [25] combines a fixed-time observer with a fractional-order phase-compensated repetitive controller, enabling efficient suppression of current loop disturbances and harmonics; however, its complex formulation leads to considerable computational burden. An adaptive repetitive learning control effectively compensates bounded periodic uncertainties but exhibits poor generalization to non-repetitive tasks [26]. A cross-coupled ILC with adaptive gain scheduling achieves nanoscale synchronization for wafer scanners but suffers from high implementation complexity [27]. For coupled or high-order systems, a high-order SMC ensures finite-time convergence and strong robustness at the cost of significant computational demand [28]. A decoupled current control with adaptive quasi-resonant and linear ESO separates the disturbances effectively, though complicating tuning and stability analysis [29]. Moreover, a cross-decoupled harmonic suppression method combining notch filters and second-order generalized integrator enhances current regulation but is frequency-sensitive [30], while a modified discrete proportional-integral-resonant (PIR) controller with prefiltering and active damping improves transient response yet relies on accurate z-domain modeling [31]. Overall, these hybrid structures combining predictive, adaptive, and observer-based designs substantially improve motor performance but remain limited by computational complexity, fast observer convergence, strong noise immunity, high parameter robustness, superior suppression of both aperiodic disturbances and periodic harmonics, and adaptive balancing of system stability margins under time-varying and complex conditions.

In this article, unlike conventional VRC, the proposed scheme introduces an adaptive fractional-order operator, which is dynamically tuned in real-time according to the load current amplitude, harmonic rejection strength, and desired phase margin. Then, compared with existing ESOs, the proposed method augments the integral of the measured current as an additional system state variable, leveraging the intrinsic low-pass filtering characteristic of the integral operator to effectively suppress high-frequency measurement noise. Moreover, a modified nonlinear error correction law is designed to ensure fixed-time convergence of the observer. Finally, the convergent behavior, system stability, disturbances and noise suppression performance are analyzed in the PMSM drive system. The main motivations of this research can be summarized as follows.

1) An adaptive fractional-order resonant controller (AFRC) is developed, featuring a self-tuning fractional-order operator that dynamically adjusts to load current amplitude, harmonic rejection strength, and desired phase margin.
2) A fixed-time augmented extended state observer (FxTAESO) is proposed, introducing an augmented current integral term to decouple the interaction between measurement noise and high observer gain.
3) A nonlinear fixed-time correction law is introduced to ensure that the state estimation error converges within a predefined time, regardless of the state initial conditions, improving both robustness and convergence rate.
4) The integrated FxTAESO-AFRC current control framework achieves enhanced harmonic suppression abilities, superior steady-state accuracy, and fast transient dynamics under both periodic and aperiodic disturbances in motor drive systems.

This paper is organized as follows. In Section II, the dynamic mathematical model and the types of current disturbances of PMSM are briefly described. In Section III, the FxTAESO-AFRC strategy is proposed to simultaneously suppress periodic and

aperiodic disturbances in the PMSM current loop. Afterwards, the corresponding proof of convergent time for FxTAESO is derived. Section IV analyzes the performance of the proposed strategy for disturbances suppression, current tracking, anti-noise capability, adaptive function design and the global system stability. Section V completes the verification for the feasibility of the algorithm through experiments. In Section VI, the conclusion is given.

II. PMSM Model Description and Disturbance Analysis

A. Dynamic Mathematical Model

Generally, by neglecting the complex nonlinearities, such as hysteresis losses, eddy currents, and iron core saturation of PMSM, dynamic mathematical equations of electrical system in the *dq*-axes are given by:

$$\begin{cases} u_d = L_d \frac{di_d}{dt} + R_s i_d - p_n \omega_m L_q i_q \\ u_q = L_q \frac{di_q}{dt} + R_s i_q + p_n \omega_m L_d i_d + p_n \omega_m \psi_f \end{cases} \tag{1}$$

where u_d, u_q, i_d, i_q, L_d and L_q are the voltages, currents, and stator inductances of the *dq*-axes, respectively; R_s represents the stator resistor; p_n denotes the number of pole pairs; ω_m is the actual mechanical angular velocity; ψ_f is the permanent magnet flux. In this study, the surface-mounted PMSM is investigated, on account of this, it holds $L_d = L_q = L_s$.

B. Current Disturbances Analysis

During the operation of an actual electrical motor, the PMSM drive system will inevitably be subjected to a range of internal and external disturbance. Before implementing the suppression techniques for these disturbances, it is essential to theoretically analyze and classify the underlying causes and characteristics of these disturbances. To enable the development of a more accurate and effective suppression strategy, these can be categorized into periodic and aperiodic types.

1) Periodic disturbances: The periodic disturbances $\varepsilon_{d(q)pd}$ are primarily associated with $\varepsilon_{d(q)fh}$ introduced by motor air-gap flux harmonics, $\varepsilon_{d(q)vh}$ caused by inverter nonlinearities, current sampling error $\varepsilon_{d(q)cs}$ and other unknown disturbances $\varepsilon_{d(q)ud}$. The expressions for the periodic disturbances in the *dq*-axes voltage equations can be summarized as:

$$\begin{cases} \varepsilon_{dpd} = \underbrace{\frac{4T_d U_{dc}}{\pi T_s L_{so}} \sum_{n=1}^{\infty} \left[\frac{12n}{36n^2-1} \sin(6n\omega_e t)\right]}_{\varepsilon_{dvh}} + \varepsilon_{dud} \\ \quad \underbrace{+\frac{\omega_e}{L_{so}} \sum_{n=1}^{\infty} \psi_{dfn} \cos(6n\omega_e t)}_{\varepsilon_{dfh}} \underbrace{-\frac{R_{so}}{L_{so}} \Delta i_d + \omega_e \Delta i_q}_{\varepsilon_{dcs}} \\ \varepsilon_{qpd} = \underbrace{\frac{4T_d U_{dc}}{\pi T_s L_{so}} \left\{-1 + \sum_{n=1}^{\infty} \left[\frac{2}{36n^2-1} \cos(6n\omega_e t)\right]\right\}}_{\varepsilon_{qvh}} + \varepsilon_{qud} \\ \quad \underbrace{+\frac{\omega_e}{L_{so}} \sum_{n=1}^{\infty} \psi_{qfn} \sin(6n\omega_e t)}_{\varepsilon_{qfh}} \underbrace{-\frac{R_{so}}{L_{so}} \Delta i_q - \omega_e \Delta i_d}_{\varepsilon_{qcs}} \end{cases} \tag{2}$$

where T_d, T_s and U_{dc} denote the deadtime interval, switching period and bus voltage of the inverter; ψ_{dfn} and ψ_{qfn} are amplitudes of the $6n^{\text{th}}$-order flux harmonics; $\omega_e = p_n \omega_m$ is the electrical angular velocity; Δi_d and Δi_q are the *dq*-axes current harmonics caused by scaling and offset error in current sampling process. The specific forms of harmonics are denoted as:

$$\begin{cases} \Delta i_d = \frac{|K_b - K_a|}{\sqrt{3}} I \sin\left(2\omega_e t - \frac{\pi}{6}\right) + \frac{\sqrt{3}(K_b - K_a)}{6} I \\ \quad + \frac{2}{\sqrt{3}} \sqrt{\Delta i_{as}^2 + \Delta i_{as} \Delta i_{bs} + \Delta i_{bs}^2} \sin(\omega_e t + \kappa) \\ \Delta i_q = \frac{|K_b - K_a|}{\sqrt{3}} I \cos\left(2\omega_e t - \frac{\pi}{6}\right) + \frac{K_a + K_b - 2}{2} I \\ \quad + \frac{2}{\sqrt{3}} \sqrt{\Delta i_{as}^2 + \Delta i_{as} \Delta i_{bs} + \Delta i_{bs}^2} \cos(\omega_e t + \kappa) \end{cases} \tag{3}$$

where K_a, K_b, Δi_{as} and Δi_{bs} are scaling coefficients and offset errors between actual and measured currents of phase-A and B. Ideally, these should meet the condition of $K_a = K_b = 1$, and $\Delta i_{as} = \Delta i_{bs} = 0$. I represents the phase current amplitude.

Based on the above analysis, it can be concluded that the periodic disturbances are mainly concentrated at the 1st, 2nd, and 6th harmonics of the fundamental frequency, which provides theoretical guidance for harmonic suppression scheme.

2) Aperiodic disturbances: The aperiodic disturbances $\varepsilon_{d(q)ad}$ primarily include cross-coupling $\varepsilon_{d(q)cc}$, the known disturbances $\varepsilon_{d(q)kd}$, parameters mismatch $\varepsilon_{d(q)pm}$, abrupt changes terms $\varepsilon_{d(q)ac}$ in reference or load, and other external uncertainties $\varepsilon_{d(q)eu}$. The aperiodic disturbances in the *dq*-axes voltage equations can be obtained as follows:

$$\begin{cases} \varepsilon_{dad} = \underbrace{\left(-\frac{\Delta L_d}{L_{so}} \frac{di_d}{dt} - \frac{\Delta R_s}{L_{so}} i_d + \omega_e \frac{\Delta L_q}{L_{so}} i_q\right)}_{\varepsilon_{dpm}} \\ \quad \underbrace{+\omega_e i_q}_{\varepsilon_{dcc}} \underbrace{-\frac{R_{so}}{L_{so}} i_d}_{\varepsilon_{dkd}} + \varepsilon_{deu} + \varepsilon_{dac} \\ \varepsilon_{qad} = \underbrace{\left(-\frac{\Delta L_q}{L_{so}} \frac{di_q}{dt} - \frac{\Delta R_s}{L_{so}} i_q - \omega_e \frac{\Delta L_d}{L_{so}} i_d - \omega_e \frac{\Delta \psi_f}{L_{so}}\right)}_{\varepsilon_{qpm}} \\ \quad \underbrace{-\omega_e i_d}_{\varepsilon_{qcc}} \underbrace{-\frac{R_{so}}{L_{so}} i_q - \omega_e \frac{\psi_{fo}}{L_{so}}}_{\varepsilon_{qkd}} + \varepsilon_{qeu} + \varepsilon_{qac} \end{cases} \tag{4}$$

where $\Delta L_d = L_d - L_{so}$, $\Delta L_q = L_q - L_{so}$, $\Delta R_s = R_s - R_{so}$ and $\Delta \psi_f = \psi_f - \psi_{fo}$. L_{so}, R_{so}, and ψ_{fo} denote the nominal values of corresponding variables.

Building upon the above disturbances analysis, the dynamic mathematical model of the current loop considering both periodic and aperiodic disturbances can be restructured as:

$$\begin{cases} \frac{di_d}{dt} = b_o u_d + \varepsilon_d \\ \frac{di_q}{dt} = b_o u_q + \varepsilon_q \end{cases} \tag{5}$$

where $\varepsilon_{d(q)} = \varepsilon_{d(q)pd} + \varepsilon_{d(q)ad}$ denotes the total disturbances of *dq*-axes, respectively. $b_o = 1/L_{so}$ is the control gain. From Eq. (5), it can be concluded that the structure of *dq*-axes dynamic model is the same. Then, this paper focuses on the *q*-axis as a typical case to facilitate the introduction of proposed algorithm. It is worth mentioning that the proposed current control strategy is still applicable for interior permanent magnet motors. According to Eq. (5), the only difference between the interior and the surface-mounted motors is that the *dq*-axis control gains are not equal, and the rest of the parts are consistent.

III. Proposed FXTAESO-AFRC Controller

To suppress the PMSM current loop periodic and aperiodic disturbances, this work proposes the novel FxTAESO-AFRC algorithm. Additionally, the stability and convergence proofs are comprehensively derived and a systematically implementation of the current control strategy is provided.

A. Design and Convergence Proof of Proposed FxTAESO

Phase currents acquisition is essential in the current control of the motor drive system. However, the acquisition process is highly

susceptible to current measurement noise arise from current sensors, analog-to-digital conversion circuits, quantization errors, and other external interference, which will be introduced into the close-loop system. Additionally, when designing a classical observer, the noise-laden current captured as an input term is also multiplicatively coupled to the high observer gain, which further exacerbates the detrimental effect of noise on observer performance. To decouple the interaction properties between current sampling noise and high observer gain, and reduce the noise sensitivity of close-loop system, the current integral term is incorporated as an augmented variable to filter measurement noise. The following augmented variable is defined as:

$$i_{qo}(t) = \int_0^t \Big(i_q(\tau) + \sigma_q(\tau) \Big) d\tau \tag{6}$$

where $i_q(t)$ and $\sigma_q(t)$ are the actual q-axis current except noise and measurement noise, respectively; $i_{qo}(t)$ is the integral term of the noisy current. It is worth mentioning that, according to Eq. (5) and Eq. (6), this integral augmented variable contains all information about disturbances and noise in the current loop. Augmenting this dummy state to a system variable and considering the higher-order derivatives of the total disturbances yield the following system state equations as:

$$\begin{cases} \dot{\boldsymbol{x}} = \boldsymbol{A_0 x} + \boldsymbol{B_0} u_q + \boldsymbol{E_0} \varepsilon_q^{(n-2)} + \boldsymbol{F_0} \sigma_q \\ y = \boldsymbol{C_0 x} \end{cases} \tag{7}$$

where $\boldsymbol{x} = \begin{bmatrix} x_1 \; x_2 \; x_3 \; \cdots \; x_n \end{bmatrix}_{1*n}^T = \begin{bmatrix} i_{q0} \; i_q \; \varepsilon_q \; \cdots \; \varepsilon_q^{(n-3)} \end{bmatrix}_{1*n}^T$, $\boldsymbol{C_0} = [0\,1\,0\,\cdots\,0]_{1*n}$, $\boldsymbol{E_0} = [0\,0\,\cdots\,0\,1]_{1*n}^T$, $\boldsymbol{F_0} = [1\,0\,\cdots\,0\,0]_{1*n}^T$, $\boldsymbol{A_0} = \begin{bmatrix} 0 & 1 & 0 & \cdots & 0 \\ 0 & 0 & 1 & \ddots & \vdots \\ \vdots & \vdots & \ddots & \ddots & 0 \\ 0 & 0 & \cdots & 0 & 1 \\ 0 & 0 & \cdots & 0 & 0 \end{bmatrix}_{n*n}$, and $\boldsymbol{B_0} = \begin{bmatrix} 0 \\ b_o \\ 0 \\ \vdots \\ 0 \end{bmatrix}_{n*1}$.

Most importantly, the (n-2)[th] derivative of the total disturbances $\varepsilon_q^{(n-2)}$ and current measurement noise σ_q exist and fulfill $\left|\varepsilon_q^{(n-2)}\right| \leq \varepsilon_{max}^{(n-2)}$ as well as $|\sigma_q| \leq \sigma_{qmax}$, where $\varepsilon_{max}^{(n-2)}$ and σ_{qmax} represent the upper limitations.

Based on this augmented state space model of PMSM [32], [33], the proposed FxTAESO is shown by:

$$\begin{cases} \dot{z}_1 = z_2 + l_1 \omega_0 \Lambda(\rho, \alpha_1, \beta_1, e_1) \\ \dot{z}_2 = z_3 + b_o u_q + l_2 \omega_0^2 \Lambda(\rho, \alpha_2, \beta_2, e_1) \\ \dot{z}_3 = z_4 + l_3 \omega_0^3 \Lambda(\rho, \alpha_3, \beta_3, e_1) \\ \vdots \\ \dot{z}_n = l_n \omega_0^n \Lambda(\rho, \alpha_n, \beta_n, e_1) \end{cases} \tag{8}$$

$$\Lambda(\rho, \alpha_i, \beta_i, e_1) = \begin{cases} \frac{(\rho^{1-\alpha_i} + \rho^{1-\beta_i}) e_1}{\rho^{2-\alpha_i-\beta_i}}, 0 \leq |e_1| < \rho \\ \lceil e_1 \rfloor^{\alpha_i} + \lceil e_1 \rfloor^{\beta_i}, |e_1| \geq \rho \end{cases} \quad i = 1,2,\ldots,n \tag{9}$$

where $\boldsymbol{z} = \begin{bmatrix} z_1 \; z_2 \; z_3 \; \cdots \; z_n \end{bmatrix}_{1*n}^T$ is the estimation value of $\boldsymbol{x}$, $e_1 = x_1 - z_1$ is the observation error of state variable x_1, ω_0 is a variable associated with the observer bandwidth, $0 < \rho < 1$ is the switching point, $\lceil \cdot \rfloor^* = sign(\cdot)|\cdot|^*$, $\alpha_i = i\alpha - i + 1, \alpha \in (1 - 1/n, 1)$, $\beta_i = i\beta - i + 1, \beta \in (1, 1 + 1/n)$, and the observer gain $\boldsymbol{L} = \begin{bmatrix} l_1 \; l_2 \; \cdots \; l_n \end{bmatrix}_{1*n}^T$ makes the following matrix $\boldsymbol{A_c}$ to be Hurwitz matrix that can be expressed by:

$$\boldsymbol{A_c} = \begin{bmatrix} -l_1\omega_0 & 1 & 0 & \cdots & 0 \\ -l_2\omega_0^2 & 0 & 1 & \ddots & \vdots \\ \vdots & \vdots & \ddots & \ddots & 0 \\ -l_{n-1}\omega_0^{n-1} & 0 & \cdots & 0 & 1 \\ -l_n\omega_0^n & 0 & \cdots & 0 & 0 \end{bmatrix}_{n*n} \tag{10}$$

This work will be divided into two scenarios for the convergence proof of proposed FxTAESO.

Case I: When $|e_1| \geq \rho$, the FxTAESO is nonlinear. Defining $\lambda_i = l_i \omega_0^i, i = 1,2,\ldots,n$, thus yields $\boldsymbol{e} \triangleq \begin{bmatrix} e_1 \; e_2 \; \cdots \; e_n \end{bmatrix}_{1*n}^T$ by:

$$\begin{cases} \dot{e}_\iota = e_{i+1} - \lambda_i \left(\lceil e_1 \rfloor^{\alpha_i} + \lceil e_1 \rfloor^{\beta_i} \right), \; i = 1,2,\ldots,n-1 \\ \dot{e}_n = -\lambda_n \left(\lceil e_1 \rfloor^{\alpha_n} + \lceil e_1 \rfloor^{\beta_n} \right) + \varepsilon_q^{(n-2)} \end{cases} \tag{11}$$

The system (11) can be further expressed as:

$$\dot{\boldsymbol{e}} \triangleq \boldsymbol{r}(\boldsymbol{e}), \qquad \boldsymbol{e}(0) = \boldsymbol{e}_0 \tag{12}$$

where $r_i(\boldsymbol{e}) = \dot{e}_\iota$, $\boldsymbol{r}(\boldsymbol{e})|_{\varepsilon_q^{(n-2)}=0}$ denotes undisturbed system (12).

The upcoming demonstration will be organized into three parts. In the first two parts, the asymptotic stability and fixed-time convergence of undisturbed system $\boldsymbol{r}(\boldsymbol{e})|_{\varepsilon_q^{(n-2)}=0}$ will be discussed. In the third part, the analysis will extend to actual fixed-time stability of the disturbed system when $\varepsilon_q^{(n-2)} \neq 0$.

Part 1: When $\varepsilon_q^{(n-2)} = 0$, system (12) can be rewritten as:

$$\dot{\boldsymbol{e}}|_{\varepsilon_q^{(n-2)}=0} = \boldsymbol{r}(\boldsymbol{e})|_{\varepsilon_q^{(n-2)}=0} = \boldsymbol{r}_\gamma(\boldsymbol{e}) = \begin{bmatrix} -\lambda_1(1+m)\lceil e_1 \rfloor^\gamma + e_2 \\ \vdots \\ -\lambda_i\left(1+m^i\right)\lceil e_1 \rfloor^{i\gamma-i+1} + e_{i+1} \\ \vdots \\ -\lambda_n(1+m^n)\lceil e_1 \rfloor^{n\gamma-n+1} \end{bmatrix}_{n*1} \tag{13}$$

where, if $\mathbf{e} \in \{\boldsymbol{e} \in \mathbb{R}^n / \{0\} : |e_1| \leq 1\}$, then $\gamma = \alpha, m = |e_1|^{\beta-\alpha}$. If $\mathbf{e} \in \{\boldsymbol{e} \in \mathbb{R}^n / \{0\} : |e_1| \geq 1\}$, then $\gamma = \beta, m = |e_1|^{\alpha-\beta}$. By using the ***Definitions*** **2** and **3** in the **Appendix**, the system $\boldsymbol{r}(\boldsymbol{e})|_{\varepsilon_q^{(n-2)}=0}$ is bi-limit homogeneous with the corresponding triples $(\boldsymbol{h}_0, d_0, \boldsymbol{f}_0)$ and $(\boldsymbol{h}_\infty, d_\infty, \boldsymbol{f}_\infty)$. In the 0-limit and ∞-limit triples, $\boldsymbol{h}_0 = \{(i-1)\alpha - (i-2)\}_{i=1}^n, d_0 = \alpha - 1$ and $\boldsymbol{h}_\infty = \{(i-1)\beta - (i-2)\}_{i=1}^n, d_\infty = \beta - 1$, or that reason, similar vector fields are

$$\boldsymbol{r}_0(\boldsymbol{e}) = \begin{bmatrix} -\lambda_1 \lceil e_1 \rfloor^\alpha + e_2 \\ \vdots \\ -\lambda_n \lceil e_1 \rfloor^{n\alpha-n+1} \end{bmatrix}_{n*1}, \boldsymbol{r}_\infty(\boldsymbol{e}) = \begin{bmatrix} -\lambda_1 \lceil e_1 \rfloor^\beta + e_2 \\ \vdots \\ -\lambda_n \lceil e_1 \rfloor^{n\beta-n+1} \end{bmatrix}_{n*1}$$

Based on the relationship between the linear and nonlinear systems [34], stability analysis of homogeneous system [35], and the Hurwitz matrix $\boldsymbol{A_c}$, it can be obtained that $\dot{\boldsymbol{e}} = \boldsymbol{r}_0$ and $\dot{\boldsymbol{e}} = \boldsymbol{r}_\infty$ are globally asymptotically stable. Similarly, the origins of $\boldsymbol{r}(\boldsymbol{e})|_{\varepsilon_q^{(n-2)}=0}$ is globally asymptotically stable.

Part 2: The origin of $\boldsymbol{r}(\boldsymbol{e})|_{\varepsilon_q^{(n-2)}=0}$ is globally asymptotically stable. Moreover, $d_\infty = \beta - 1 > 0 > \alpha - 1 = d_0$. So, the origin system is fixed-time convergent according to ***Lemma*** **1** in **Appendix**. There exists a continuous, positive definite and proper Lyapunov function $V(\boldsymbol{e})$. Defining by:

$$\begin{cases} \mu(\boldsymbol{e}) \triangleq V(\boldsymbol{e})^{\frac{d_{V_0}+d_0}{d_{V_0}}} + V(\boldsymbol{e})^{\frac{d_{V_\infty}+d_\infty}{d_{V_\infty}}} \\ \delta(\boldsymbol{e}) \triangleq -\dot{V}(\boldsymbol{e}) = -\frac{\partial V(\boldsymbol{e})}{\partial \boldsymbol{e}} \boldsymbol{r}(\boldsymbol{e})|_{\varepsilon_q^{(n-2)}=0} \\ d_{V_0} > \max_{1 \leq i \leq n} \boldsymbol{h}_{0,i} = 1, d_{V_\infty} > \max_{1 \leq i \leq n} \boldsymbol{h}_{\infty,i} = (n-1)\beta - (n-2) \\ d_0 = \alpha - 1 < 0, \quad d_\infty = \beta - 1 > 0 \end{cases} \tag{14}$$

The $\delta(\boldsymbol{e})$ and $\mu(\boldsymbol{e})$ are bi-limit homogeneous. Based on ***Lemma*** **2** in **Appendix**, a positive real number p_V makes:

$$\left(V(\boldsymbol{e})^{(d_{V_0}+d_0)/d_{V_0}} + V(\boldsymbol{e})^{(d_{V_\infty}+d_\infty)/d_{V_\infty}} \right) \leq -\frac{\boldsymbol{r}(\boldsymbol{e})|_{\varepsilon_q^{(n-2)}=0}}{p_V} \frac{\partial V(\boldsymbol{e})}{\partial \boldsymbol{e}} \tag{15}$$

Based on the quantitative relationship $\left(d_{V_\infty} + d_\infty\right) \Big/ d_{V_\infty} > 1 > \left(d_{V_0} + d_0\right) \Big/ d_{V_0}$ of the variables, (15) can be redesigned as:

$$\dot{V}(\boldsymbol{e}) = \frac{\partial V(\boldsymbol{e})}{\partial \boldsymbol{e}} \boldsymbol{r}(\boldsymbol{e})|_{\varepsilon_q^{(n-2)}=0} \leq \begin{cases} -p_V V(\boldsymbol{e})^{\frac{d_{V_\infty}+d_\infty}{d_{V_\infty}}}, V(\boldsymbol{e}) \geq 1 \\ -p_V V(\boldsymbol{e})^{\frac{d_{V_0}+d_0}{d_{V_0}}}, V(\boldsymbol{e}) \leq 1 \end{cases} \tag{16}$$

Thus, the convergence time t_1 of system $\boldsymbol{r}(\boldsymbol{e})|_{\varepsilon_q^{(n-2)}=0}$ meets:

$$t_1 \le \frac{1}{p_V}\left(d_{V_0}/(1-\alpha) + d_{V_\infty}/(\beta-1)\right)t_{ini} = t_{max1} \quad (17)$$

where t_{ini} is a positive real number associated with $V(\boldsymbol{e}_0)$.

Part 3: When $\varepsilon_q^{(n-2)} \neq 0$ and $\left|\varepsilon_q^{(n-2)}\right| < \varepsilon_{max}^{(n-2)}$, the Lyapunov function $V(\boldsymbol{e})$ can be rewritten by:

$$\dot{V}(\boldsymbol{e}) = \frac{\partial V(\boldsymbol{e})}{\partial \boldsymbol{e}}\, \boldsymbol{r}(\boldsymbol{e})|_{\varepsilon_q^{(n-2)}=0} + \frac{\partial V(\boldsymbol{e})}{\partial e_n}\varepsilon_q^{(n-2)} \quad (18)$$

Then the bi-limit homogeneous functions can be defined based on ***Lemma* 1** in **Appendix** as:

$$\begin{cases} \mu_\Delta(\boldsymbol{e}) = |\partial V(\boldsymbol{e})/\partial e_n| \\ \delta_\Delta(\boldsymbol{e}) = V(\boldsymbol{e})^{(d_{V_0}-\boldsymbol{h}_{0,n})/d_{V_0}} + V(\boldsymbol{e})^{(d_{V_\infty}-\boldsymbol{h}_{\infty,n})/d_{V_\infty}} \end{cases} \quad (19)$$

where $\mu_\Delta(\boldsymbol{e})$ and $\delta_\Delta(\boldsymbol{e})$ are bi-limit homogeneous with weight $\boldsymbol{h}_q$ and degree $d_{V_q} - h_{q,n}, q = 0\ or\ \infty$. Based on ***Lemma* 2** in **Appendix** and the relationship $\left(d_{V_\infty} - h_{\infty,n}\right)/d_{V_\infty} > \left(d_{V_0} - h_{0,n}\right)/d_{V_0} > 0$, there is a positive real number p_Δ makes:

$$\left|\frac{\partial V(\boldsymbol{e})}{\partial e_n}\right| \le p_\Delta\left(V(\boldsymbol{e})^{(d_{V_0}-\boldsymbol{h}_{0,n})/d_{V_0}} + V(\boldsymbol{e})^{(d_{V_\infty}-\boldsymbol{h}_{\infty,n})/d_{V_\infty}}\right) \quad (20)$$

The collation can be further obtained as:

$$\left|\frac{\partial V(\boldsymbol{e})}{\partial e_n}\varepsilon_q^{(n-2)}\right| \le \begin{cases} 2p_\Delta V(\boldsymbol{e})^{(d_{V_\infty}-\boldsymbol{h}_{\infty,n})/d_{V_\infty}}\varepsilon_{max}^{(n-2)}, V(\boldsymbol{e}) \ge 1 \\ 2p_\Delta V(\boldsymbol{e})^{(d_{V_0}-\boldsymbol{h}_{0,n})/d_{V_0}}\varepsilon_{max}^{(n-2)}, V(\boldsymbol{e}) \le 1 \end{cases} \quad (21)$$

Combining Eq. (14) and Eq. (21) in Eq. (18) yields:

$$\dot{V}(\boldsymbol{e}) \le \begin{cases} -\left(p_V V(\boldsymbol{e})^{(d_{V_0}+d_0)/d_{V_0}} - 2p_\Delta\varepsilon_{max}^{(n-2)}V(\boldsymbol{e})^{(d_{V_\infty}-\boldsymbol{h}_{\infty,n})/d_{V_\infty}}\right) \\ -p_V V(\boldsymbol{e})^{(d_{V_\infty}+d_\infty)/d_{V_\infty}}, V(\boldsymbol{e}) \ge 1 \\ -\left(p_V V(\boldsymbol{e})^{(d_{V_\infty}+d_\infty)/d_{V_\infty}} - 2p_\Delta\varepsilon_{max}^{(n-2)}V(\boldsymbol{e})^{(d_{V_0}-\boldsymbol{h}_{0,n})/d_{V_0}}\right) \\ -p_V V(\boldsymbol{e})^{(d_{V_0}+d_0)/d_{V_0}}, V(\boldsymbol{e}) \le 1 \end{cases} \quad (22)$$

Making the following inequalities hold:

$$\begin{cases} p_V V(\boldsymbol{e})^{(d_{V_0}+d_0)/d_{V_0}} - 2p_\Delta\varepsilon_{max}^{(n-2)}V(\boldsymbol{e})^{(d_{V_\infty}-\boldsymbol{h}_{\infty,n})/d_{V_\infty}} \ge 0 \\ p_V V(\boldsymbol{e})^{(d_{V_\infty}+d_\infty)/d_{V_\infty}} - 2p_\Delta\varepsilon_{max}^{(n-2)}V(\boldsymbol{e})^{(d_{V_0}-\boldsymbol{h}_{0,n})/d_{V_0}} \ge 0 \end{cases} \quad (23)$$

Then

$$\begin{cases} V(\boldsymbol{e}) \ge \left(2p_\Delta\varepsilon_{max}^{(n-2)}/p_V\right)^{d_{V_0}d_{V_\infty}/(d_{V_\infty}d_0 + d_{V_0}\boldsymbol{h}_{\infty,n})} = V_1 \\ V(\boldsymbol{e}) \ge \left(2p_\Delta\varepsilon_{max}^{(n-2)}/p_V\right)^{d_{V_0}d_{V_\infty}/(d_{V_0}d_\infty + d_{V_\infty}\boldsymbol{h}_{0,n})} = V_2 \end{cases} \quad (24)$$

If $2p_\Delta Q/p_V \ge 1$, then $V_1 \ge 1$ and $V_2 \ge 1$. By combining Eq. (22), Eq. (24), the Eq. (25) can be obtained by:

$$\dot{V}(\boldsymbol{e}) \le -p_V V(\boldsymbol{e})^{(d_{V_\infty}+d_\infty)/d_{V_\infty}}, \quad V(\boldsymbol{e}) \ge V_1 \quad (25)$$

The convergence time t_2 from $V(\boldsymbol{e}_0)$ to V_1 is:

$$t_2 \le \frac{d_{V_\infty}}{p_V d_\infty}\left(\frac{1}{V_1^{d_\infty/d_{V_\infty}}} - \frac{1}{V(\boldsymbol{e}_0)^{d_\infty/d_{V_\infty}}}\right) \le \frac{d_{V_\infty}}{p_V d_\infty}\frac{1}{V_1^{d_\infty/d_{V_\infty}}} = t_{max2} \quad (26)$$

Therefore, the error $\boldsymbol{e}$ will gradually converge to the vicinity of the origin $\Theta_1 = \{\boldsymbol{e} \in \mathbb{R}^n |\ V(\boldsymbol{e}) \le V_1\}$ within finite time t_2.

On the other hand, if $2p_\Delta Q/p_V < 1$, then $V_1 < 1$ and $V_2 < 1$. The Eq. (22) can be rewritten as:

$$\dot{V}(\boldsymbol{e}) \le \begin{cases} -p_V V(\boldsymbol{e})^{(d_{V_\infty}+d_\infty)/d_{V_\infty}}, V(\boldsymbol{e}) \ge 1 \\ -p_V V(\boldsymbol{e})^{(d_{V_0}+d_0)/d_{V_0}}, V_2 \le V(\boldsymbol{e}) < 1 \end{cases} \quad (27)$$

The convergence time t_3 from $V(\boldsymbol{e}_0)$ to V_2 is:

$$t_3 \le \frac{d_{V_\infty}}{p_V d_\infty}\left(1 - \frac{1}{V(\boldsymbol{e}_0)^{d_\infty/d_{V_\infty}}}\right) + \frac{d_{V_0}}{p_V|d_0|}\left(1 - V_2^{|d_0|/d_{V_0}}\right) \le \frac{1}{p_V}\left(\frac{d_{V_\infty}}{d_\infty} + \frac{d_{V_0}}{|d_0|}\right) = t_{max3} \quad (28)$$

Thus, the vector $\boldsymbol{e}$ will gradually converge to the vicinity of origin $\Theta_2 = \{\boldsymbol{e} \in \mathbb{R}^n |\ V(\boldsymbol{e}) \le V_2\}$ within finite time t_3.

In brief, the observation error $\boldsymbol{e}$ will converge to 0 gradually within finite time $t_1 \le t_{max1}$ when $\varepsilon_q^{(n-2)} = 0$. Otherwise, it will converge to the vicinity of origin $\Theta = \left\{\boldsymbol{e} \in \mathbb{R}^n | \boldsymbol{e} \in \Theta_1\right\} \cup \left\{\boldsymbol{e} \in \mathbb{R}^n | \boldsymbol{e} \in \Theta_2\right\}$ gradually within finite time t_4, where t_4 is uniformly bounded by $max\{t_{max2}, t_{max3}\}$.

Based on the above convergent proofs, it's known that the observation error vector $\boldsymbol{e}$ of the FxTAESO can converge to the switching point $|e_1| = \rho$ in a fixed time when $2p_\Delta Q/p_V < 1$ and $V_2 \le V\left(\left[\rho\ e_2\ \cdots\ e_n\right]_{1*n}^T\right)$ is set artificially.

Case II: When $0 \le |e_1| < \rho$, the FxTAESO is linear. Combining Eq. (7) and Eq. (8), we can deduce that:

$$\dot{\boldsymbol{e}} = \boldsymbol{A}_e\boldsymbol{e} + \boldsymbol{E}\varepsilon_q^{(n-2)} + \boldsymbol{F}\sigma_q$$

$$\boldsymbol{A}_e = \begin{bmatrix} -\lambda_1 Y_1 & 1 & 0 & \cdots & 0 \\ -\lambda_2 Y_2 & 0 & 1 & \ddots & \vdots \\ \vdots & \vdots & \ddots & \ddots & 0 \\ -\lambda_{n-1} Y_{n-1} & 0 & \cdots & 0 & 1 \\ -\lambda_n Y_n & 0 & \cdots & 0 & 0 \end{bmatrix}_{n*n}$$

$$Y_i = \left(\delta^{1-\alpha_i} + \delta^{1-\beta_i}\right)/\delta^{2-\alpha_i-\beta_i}, i = 1,2,\dots,n \quad (29)$$

And the observer gain matrix $\boldsymbol{L}$ can be chosen as:

$$l_i = \frac{n!}{i!(n-i)!}, \quad i = 1,2,\dots,n \quad (30)$$

Apparently, $\boldsymbol{A_e}$ is a Hurwitz matrix. Therefore, $\boldsymbol{e}$ is asymptotically stable when $\varepsilon_q^{(n-2)} = 0$. And $\boldsymbol{e}$ is bounded-input bounded-output (BIBO) stable if $\varepsilon_q^{(n-2)} \neq 0$. Based upon the deliberations of ***Case I*** and ***II***, the proposed FxTAESO has global convergence. When the observation error e_1 is large, it will initially converge to the switching point $|e_1| = \rho$ within a fixed-time by the proposed nonlinear correction term. Subsequently, it will converge to the equilibrium points or their vicinities with a linear correction term. This approach improves both dynamic response and steady-state anti-disturbance performance.

B. Design and Rational Approximation of Proposed AFRC

The quasi-vector resonant controller (QVRC) introduces the plant information and eliminates the poles of controlled object, which enhances the phase margin of system to some extent and expands the resonant bandwidth. However, the resonant gain is still insufficient. The limitation reduces controller's ability to reject periodic disturbances and weakens the system stability. To address these issues, this paper proposes an optimization of the QVRC by introducing an adaptive fractional-order term into the numerator of the controller. According to the controller form, the resonant gain is proportional to the fractional-order exponential term, but the system stability margin is inversely proportional to it. Building upon the analysis of disturbance in Section II-B, when the load current is large, the amplitudes of harmonics are large, and then the fractional-order exponential term will be increased to enhance the harmonics suppression capability. Additionally, when the load current is small, the harmonic amplitudes are also reduced accordingly, so the fractional-order exponential term can be decreased to improve the system stability. Thus, the proposed AFRC scheme can adaptively adjust the resonant gain and stability margin according to the load conditions, and AFRC is denoted by:

$$\begin{cases} G_{AFRC}^{\Delta}(s) = \frac{k_r\omega_c s^\xi(L_{so}s + R_{so})}{s^2 + \omega_c s + \omega_h^2} \\ \xi = f\left(i_q, HRS, DPM\right) \end{cases} \quad (31)$$

where ω_c and ω_h are damping and resonant frequencies, respectively. k_r is the resonant gain. $\xi \in [1,2]$ denotes adaptive fractional-order exponential term, which is determined by q-axis output current i_q, harmonic rejection strength (HRS), and close-loop system desired phase margin (DPM) in $f(*)$ function adaptively. The specific design solutions will be given in Section IV-F below.

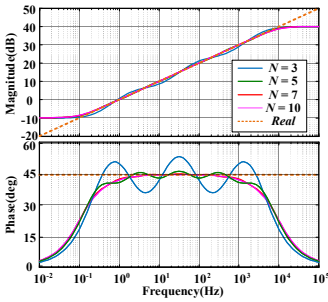

Fig. 1. Fitting results of $s^{0.5}$ with ORA method under different orders of N.

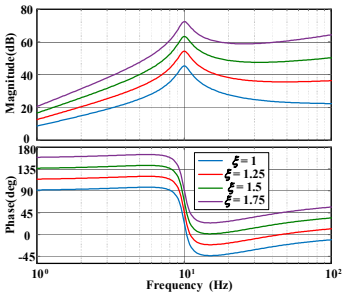

Fig. 2. The Bode plot of AFRC with varying ξ with $\omega_c = 10rad/s$ and $k_r = 300$.

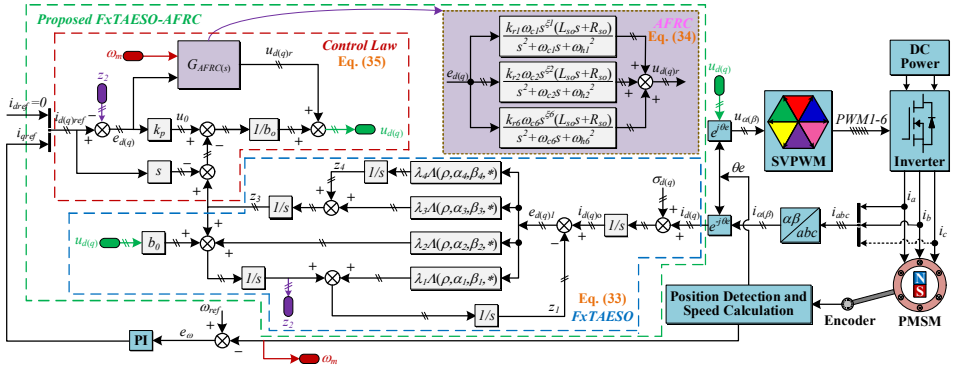

Fig. 3. The block diagram of control structure for PMSM based on field-oriented control (FOC) and proposed FxTAESO-AFRC.

Given computational challenges of implementing fractional-order calculus on a digital system, a rationalized approximation of fractional-order differential term $s^\tau, \tau = \xi - 1 \in [0,1]$ is required for the physical implementation of the actual system. To achieve this, Oustaloup Recursive Approximation (ORA) representation with high accuracy is used [36], denoted as:

$$\begin{cases} s^\tau = Y(s) = \lim\limits_{N\to\infty} (\omega_u)^\tau \prod_{k=1}^{N} \frac{1+s/\omega_k'}{1+s/\omega_k} \\ \omega_k' = \omega_l \left(\frac{\omega_u}{\omega_l}\right)^{(2k-2-\tau)/2N} \\ \omega_k = \omega_l \left(\frac{\omega_u}{\omega_l}\right)^{(2k+\tau)/2N} \end{cases} \tag{32}$$

where N is the ORA approximation order. ω_u and ω_l are upper and lower limitations of the frequency band for the ORA.

Fig. 1 compares the ORA fitting results and their theoretical amplitude-phase-frequency characteristics curves for $s^{0.5}$ with different orders N, where the frequency band is chosen as $2\pi * (10^{-1}, 10^4) rad/s$. The fitting accuracy improves as the order N increases, but the resulting transfer function becomes more complicated. The amplitude-frequency characteristic slope of the fitting result closely approximates +10dB/dec for $N = 5$, and phase-frequency characteristic remains nearly to 45° within fitting frequency band, aligning with the theoretical behavior. In Fig. 2, the influence of varying ξ when $\omega_c = 10rad/s$ and $k_r = 300$ to AFRC is exhibited. The resonant gain is greatly improved by the introduction of fractional-order term ξ, but it will also change the closed-loop system stability margin. Thus, unlike the previous two parameters ω_c and k_r, ξ can adjust both gain and phase margin of the entire system, providing an additional degree of freedom for resonant controller design. The above analysis further highlights the advantages of proposed AFRC over the conventional QVRC.

C. *Implementation of FxTAESO-AFRC in Control System*

Building upon previous analysis, it is apparent that increasing the order n of the FxTAESO improves the prediction accuracy and rejection capabilities for aperiodic disturbances. However, this comes at the cost of increasing computational complexity of the algorithm. Therefore, there is a trade-off in the selection of order n. In this paper, $n = 4$ has been selected to construct the observer, which can be redesigned as:

$$\begin{cases} \dot{z}_1 = z_2 + l_1\omega_0\Lambda(\rho,\alpha_1,\beta_1,e_1) \\ \dot{z}_2 = z_3 + b_o u_q + l_2\omega_0^2\Lambda(\rho,\alpha_2,\beta_2,e_1) \\ \dot{z}_3 = z_4 + l_3\omega_0^3\Lambda(\rho,\alpha_3,\beta_3,e_1) \\ \dot{z}_4 = l_4\omega_0^4\Lambda(\rho,\alpha_4,\beta_4,e_1) \end{cases} \tag{33}$$

where $l_1 = 4$, $l_2 = 6$, $l_3 = 4$ and $l_4 = 1$. For the periodic disturbances, Section II-B has been derived analytically that harmonics of the 1st, 2nd, and 6th fundamental frequencies are predominantly present in the current loop of the dq-axes. Hence the proposed AFRC can be rewritten as:

$$G_{AFRC}(s) = \sum_{i=1,2,6} \frac{k_{ri}\omega_{ci}s^{\xi_i}(L_{so}s+R_{so})}{s^2+\omega_{ci}s+\omega_{hi}^2} \tag{34}$$

where k_{ri}, ω_{ci}, ξ_i, and $\omega_{hi} = i\omega_e$ are the 1st, 2nd, and 6th resonant gains, damping frequencies, fractional-order term, and resonant frequencies, respectively. Based on feedback control law, estimated disturbances, resonant controller output above, and simultaneously considering the bus voltage limitations of the inverter within the linear modulation zone during practical engineering applications [37], the generalized control law of the PMSM current loop is:

$$\begin{cases} u_{q\_ini} = \frac{\dot{i}_{qref} + k_{qp}(i_{qref} - z_2) - z_3 + b_o u_{qr}}{b_o} \\ u_{qmax} = \frac{U_{dc}}{\sqrt{3}} \cdot \frac{u_{q\_ini}}{\sqrt{u_{d\_ini}^2 + u_{q\_ini}^2}} \\ \begin{cases} u_q = u_{q\_ini}, & \sqrt{u_{d\_ini}^2 + u_{q\_ini}^2} \le U_{dc}/\sqrt{3} \\ u_q = u_{qmax}, & \sqrt{u_{d\_ini}^2 + u_{q\_ini}^2} > U_{dc}/\sqrt{3} \end{cases} \end{cases} \tag{35}$$

where k_{qp} and u_{qr} are feedback gain and the form of $G_{AFRC}(s) \bullet e_q(s)$ in time-domain, respectively. u_{d_ini} and u_{q_ini} denote the preliminary calculation of the dq-axis reference voltage. u_{qmax} is q-axis maximum saturation voltage. And u_q is the reference voltage that is ultimately applied to the motor. The block diagram of control structure for PMSM based on field-oriented control (FOC) and proposed FxTAESO-AFRC is shown in Fig. 3. The FxTAESO and AFRC are configured in parallel to form the generalized control law, which produces voltage to drive motor.

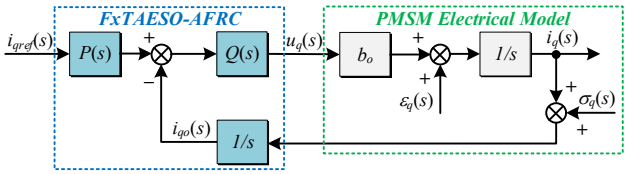

Fig. 4. The equivalent structural block diagram of the proposed FxTAESO-AFRC.

IV. Performance Analysis of the FxTAESO-AFRC

This section comprehensively analyzes the stability of entire current closed-loop control system, disturbance suppression performance, current tracking, anti-noise capability, parameters robustness and adaptive function design guidelines in $\xi = f\left(i_q, HRS, DPM\right)$ of the proposed FxTAESO-AFRC strategy.

A. Stability Analysis of Current Closed-loop System

Referring to Eq. (33)-Eq. (35), the transfer function between current controller output u_q and reference current i_{qref} and integral augmented variable i_{qo} can be obtained as Eq. (36). Where the transfer function $A(s) = s^4 + \lambda_1 M_1(E_1)s^3 + \lambda_2 M_2(E_1)s^2 + \lambda_3 M_3(E_1)s + \lambda_4 M_4(E_1)$; $M_i(E_1), i = 1,2,3,4$ is the descriptive function of nonlinear correction term $\Lambda(\rho, \alpha_i, \beta_i, e_1), i = 1,2,3,4$. In deriving a descriptive function, it is necessary to find the integral value of a sinusoidal function with different powers. And since α_i and β_i in function $\Lambda(\rho, \alpha_i, \beta_i, e_1)$ are fractional-order operators, directly calculating its integral value during the derivation process of descriptive function is challenging. Therefore, the value of the partial integral is approximated by the area enclosed by this nonlinear fractional-order function, then represented by a polynomial approximation fitting [38].

Based on this, the equivalent structural block diagram of the proposed FxTAESO-AFRC can be simplified as shown in Fig. 4. In Fig. 4, $P(s)$ is the reference prefilter, and $Q(s)$ denotes the equivalent current controller. They can be deduced as Eq. (37). Then the open-loop transfer function of the current control system based on the FxTAESO-AFRC can be displayed as follows:

$$G_{op}(s) = Q(s)b_o/s^2 \tag{38}$$

The closed-loop system stability is closely related to the variable parameters k_r, ω_c, ξ, k_{qp}, ω_0, and E_1. The Nyquist diagram of open-loop transfer function is used to demonstrate in detail the influence of each variable on the stability. Fig. 5 shows the Nyquist curves of equivalent current loop based on proposed strategy under different parameters variation. The following parameters satisfy $k_{ri} = ik_{r1}$, $\omega_{ci} = i\omega_{c1}$, and $\omega_{hi} = i\omega_{h1}, i = 1,2,6$. From Nyquist stability criterion, the number of clockwise and counterclockwise revolutions around the critical point (-1, 0) should strictly satisfy that $P = 2\left(N_+ - N_-\right)$ if the closed-loop system is to be stable, where P is the number of poles of $G_{op}(s)$ in right half s-plane, N_+ and N_- represent the laps of clockwise and counterclockwise. The above stability criterion is satisfied for all six parameter variations shown in Fig. 5, indicating that the closed-loop system is absolutely stable with low sensitivity to individual adjustable parameters. This also verifies that the proposed FxTAESO-AFRC can maintain current closed-loop system stability while effectively suppressing the current disturbances and uncertainties.

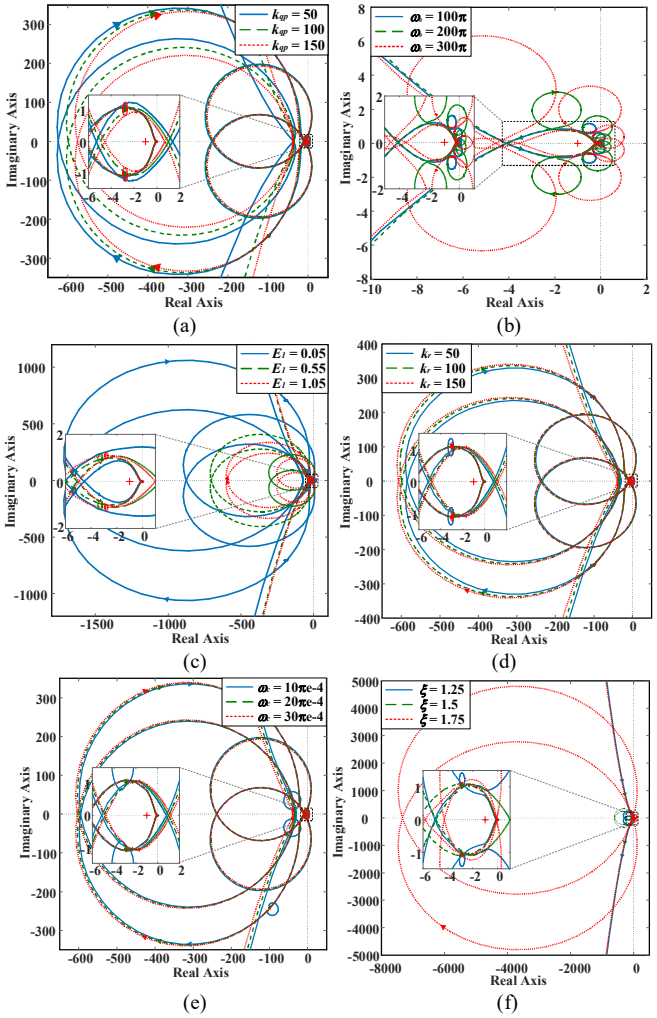

Fig. 5. The Nyquist curves of the equivalent current loop based on proposed FxTAESO-AFRC. (a) $k_{r1} = 100$, $\omega_c = 0.002\pi$, $\xi = 1.5$, $\omega_0 = 200\pi$, $\omega_{h1} = 20\pi$, and $E_1 = 1$; (b) $k_{r1} = 100$, $\omega_c = 0.002\pi$, $\xi = 1.5$, $k_{qp} = 100$, $\omega_{h1} = 20\pi$, and $E_1 = 1$; (c) $k_{r1} = 100$, $\omega_c = 0.002\pi$, $\xi = 1.5$, $k_{qp} = 100$, $\omega_{h1} = 20\pi$, and $\omega_0 = 200\pi$; (d) $\omega_0 = 200\pi$, $\omega_c = 0.002\pi$, $\xi = 1.5$, $k_{qp} = 100$, $\omega_{h1} = 20\pi$, and $E_1 = 1$; (e) $k_{r1} = 100$, $k_{qp} = 100$, $\xi = 1.5$, $\omega_0 = 200\pi$, $\omega_{h1} = 20\pi$, and $E_1 = 1$; (f) $k_{r1} = 100$, $k_{qp} = 100$, $\omega_c = 0.002\pi$, $\omega_0 = 200\pi$, $\omega_{h1} = 20\pi$, and $E_1 = 1$.

B. Disturbances Suppression Capability of FxTAESO

As the core part of the proposed disturbance suppression approach, the ability of FxTAESO to predict the aperiodic disturbances and the slow-varying disturbances determines the accuracy of the feedforward compensation in the control law. This in turn affects the final disturbance rejection performance. Therefore, based on Eq. (5) and Eq. (33), the transfer function of disturbance prediction error can be deduced as:

$$G_{\varepsilon e}(s) = \frac{z_3(s) - \varepsilon_q(s)}{\varepsilon_q(s)} = -\frac{s^4 + \lambda_1 M_1(E_1)s^3 + \lambda_2 M_2(E_1)s^2}{A(s)} \tag{39}$$

$$u_q(s) = \frac{A(s)\left(s + k_{qp} + b_o \mathrm{G}_{AFRC}(s)\right)}{b_o s^2\left[\left(s + k_{qp} + b_o \mathrm{G}_{AFRC}(s)\right)\left(s + \lambda_1 M_1(E_1)\right) + \lambda_2 M_2(E_1)\right]} i_{qref}(s) - \frac{\left(\lambda_3 M_3(E_1)s + \lambda_4 M_4(E_1)\right)\left(s + k_{qp} + b_o \mathrm{G}_{AFRC}(s)\right)s + \lambda_2 M_2(E_1)\left(k_{qp} + b_o \mathrm{G}_{AFRC}(s)\right)s^3}{b_o s^2\left[\left(s + k_{qp} + b_o \mathrm{G}_{AFRC}(s)\right)\left(s + \lambda_1 M_1(E_1)\right) + \lambda_2 M_2(E_1)\right]} i_{qo}(s) \tag{36}$$

$$\begin{cases} P(s) = \dfrac{A(s)\left(s + k_{qp} + b_o \mathrm{G}_{AFRC}(s)\right)}{\left(\lambda_3 M_3(E_1)s + \lambda_4 M_4(E_1)\right)\left(s + k_{qp} + b_o \mathrm{G}_{AFRC}(s)\right)s + \lambda_2 M_2(E_1)\left(k_{qp} + b_o \mathrm{G}_{AFRC}(s)\right)s^3} \\ Q(s) = \dfrac{\left(\lambda_3 M_3(E_1)s + \lambda_4 M_4(E_1)\right)\left(s + k_{qp} + b_o \mathrm{G}_{AFRC}(s)\right)s + \lambda_2 M_2(E_1)\left(k_{qp} + b_o \mathrm{G}_{AFRC}(s)\right)s^3}{b_o s^2\left[\left(s + k_{qp} + b_o \mathrm{G}_{AFRC}(s)\right)\left(s + \lambda_1 M_1(E_1)\right) + \lambda_2 M_2(E_1)\right]} \end{cases} \tag{37}$$

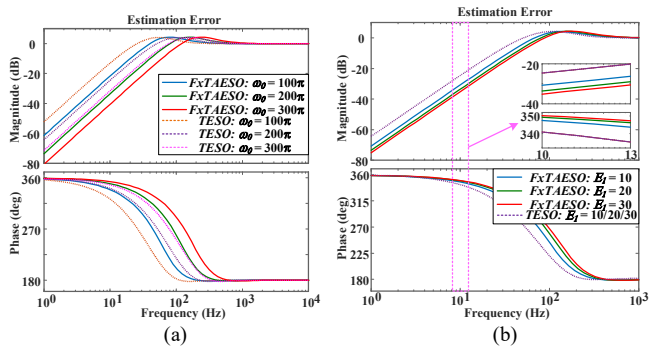

(a) (b)

Fig. 6. The bode plots of $G_{\varepsilon e}(s)$ for different error amplitudes E_1 and observer bandwidths ω_0 using TESO and proposed FxTAESO. (a) $G_{\varepsilon e}(s)$: $E_1 = 20$; (b) $G_{\varepsilon e}(s)$: $\omega_0 = 200\pi$.

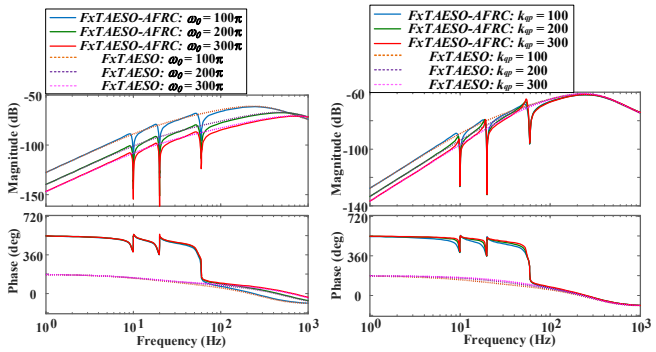

(a) (b)

Fig. 7. The bode plots of $G_{\varepsilon i}(s)$ for FxTAESO alone and the composite method FxTAESO-AFRC for different parameters variation. (a) $k_{r1} = 100$, $\omega_c = 0.002\pi$, $\xi = 1.5$, $k_{qp} = 100$, $\omega_{h1} = 20\pi$, and $E_1 = 1$; (b) $k_{r1} = 100$, $\omega_c = 0.002\pi$, $\xi = 1.5$, $\omega_0 = 200\pi$, $\omega_{h1} = 20\pi$, and $E_1 = 1$.

Building upon Eq. (39), the final value theorem can be used to analyze as follows: If $\varepsilon_q(t)$ is a constant disturbance or ramp uncertainty, it can be deduced that disturbance prediction error $\lim_{t\to\infty} e_{\varepsilon e}(t) = \lim_{s\to 0} sG_{\varepsilon e}(s)\varepsilon_q(s) = 0$. When $\varepsilon_q(t)$ is an accelerated disturbance, then disturbance prediction error will ultimately have a steady-state error. This also verifies that FxTAESO can be used to estimate aperiodic and slow-varying disturbances accurately. It's worth mentioning that the periodic disturbances are handled by the AFRC part, which has been discussed above.

To further assess the effect of different parameters on the disturbances prediction, Fig. 6 illustrates the Bode plots of $G_{\varepsilon e}(s)$ for different error amplitudes E_1 and observer bandwidths ω_0 using traditional ESO (TESO) and the proposed FxTAESO, respectively. From Fig. 6, it can be seen that for the estimation error amplitude, the proposed FxTAESO demonstrates a lower estimation error compared to TESO under the same observer bandwidth. And as the observer bandwidth ω_0 and estimation error magnitude E_1 increase, the disturbances estimation performance of FxTAESO strengthens, resulting in a reduced estimation error magnitude. This further validates the superior disturbances estimation performance of the proposed FxTAESO strategy.

To evaluate immunity performance of proposed FxTAESO-AFRC strategy, based on the equivalent control block diagram identified in Fig. 4, the transfer function from composite disturbances $\varepsilon_q(t)$ to output current $i_q(t)$ can be obtained as:

$$G_{\varepsilon i}(s) = \frac{i_q(s)}{\varepsilon_q(s)} = \frac{1/s}{1+Q(s)b_0/s^2} = \frac{s}{s^2+Q(s)b_0} \tag{40}$$

Fig. 7 draws comparison of the Bode plots of disturbances on output $G_{\varepsilon i}(s)$ for FxTAESO alone and the proposed composite method FxTAESO-AFRC for different parameters variation. It's found that high-frequency characteristics of both controllers are identical while low-frequency parts have some difference. As demonstrated in the previous analysis, the FxTAESO has strong

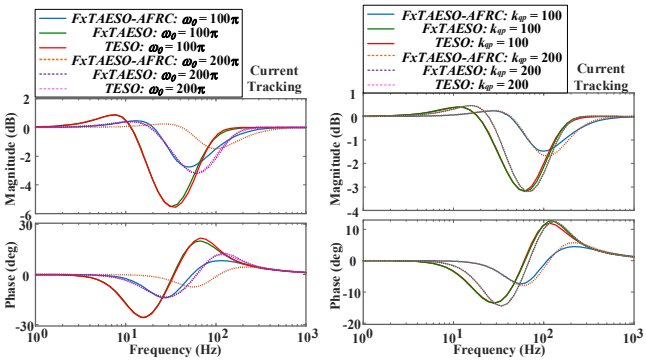

(a) (b)

Fig. 8. The bode plots of $G_{ci}(s)$ of TESO, FxTAESO alone, and the proposed FxTAESO-AFRC under different parameters variation. (a) $k_{r1} = 100$, $\omega_c = 0.002\pi$, $\xi = 1.5$, $k_{qp} = 100$, $\omega_{h1} = 20\pi$, and $E_1 = 1$; (b) $k_{r1} = 100$, $\omega_c = 0.002\pi$, $\xi = 1.5$, $\omega_0 = 200\pi$, $\omega_{h1} = 20\pi$, and $E_1 = 1$.

rejection capability for aperiodic and slow-varying disturbances, but its performance in suppression periodic disturbances is less effective. Therefore, the proposed FxTAESO-AFRC demonstrates enhanced suppression capability for harmonics at specific frequency points, while maintaining the same rejection features as FxTAESO at other frequency points. Additionally, the rejection ability of the controller is proportional to observer bandwidth ω_0 and proportional gain k_{qp}. In conclusion, the proposed FxTAESO-AFRC has superiority in suppressing both periodic and aperiodic current disturbances and harmonics.

C. *Performance of Current Tracking*

While maintaining the excellent periodic and aperiodic disturbances and uncertainties rejection capabilities of the current loop of PMSM system, the current tracking performance should not be neglected, which is critical to achieve the high-precision and fast-dynamic current response. Additionally, based on the equivalent control block diagram determined in Fig. 4, the transfer function of the current closed-loop system can be derived as

$$G_{ci}(s) = \frac{i_q(s)}{i_{qref}(s)} = \frac{P(s)Q(s)s}{L_{so}s^2+R_{so}s+Q(s)} \tag{41}$$

Similarly, the Bode plots of TESO, FxTAESO alone, and the proposed FxTAESO-AFRC are compared in the Fig. 8 to validate the superior current tracking ability of the proposed strategy in wider frequency-domain.

As can be seen from Fig. 8, the command current is accurately tracked by all three schemes at low frequencies. However, within the frequency band of 10-100Hz, both TESO and FxTAESO alone exhibit large tracking amplitude fluctuations, while the proposed FxTAESO-AFRC method has the smallest amplitude and phase fluctuations. This indicates that the proposed method can track the reference signal better in this frequency band with close to unit gain and 0° phase. In addition, increasing the observer bandwidth can further improve the current tracking performance, while adjusting the controller proportional has minor effect. Therefore, the proposed FxTAESO-AFRC offers superior current tracking performance across wider frequency-domain through the above analysis.

D. *Anti-noise Performance Comparison of FxTAESO*

This section concentrates on evaluating the enhancement of noise-rejection capability achieved by the proposed integral augmented scheme in comparison with the conventional observer approach. The s-domain transfer function that characterizes the relationship between the measurement noise $\sigma_q(s)$ and the output current $i_q(s)$ can be obtained from Fig. 4 and is expressed as follows:

$$G_{\sigma i}(s) = -\frac{b_0Q(s)}{s^2+b_0Q(s)} \tag{42}$$

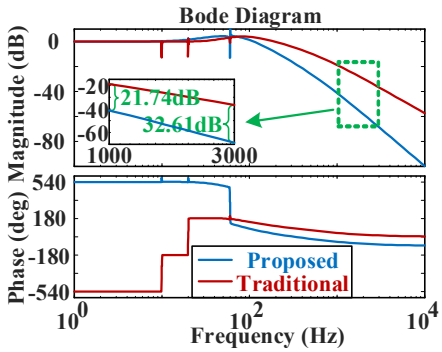

Fig. 9. The bode plots of transfer function $G_{\sigma i}(s)$ for noise immunity comparison between proposed and traditional observer.

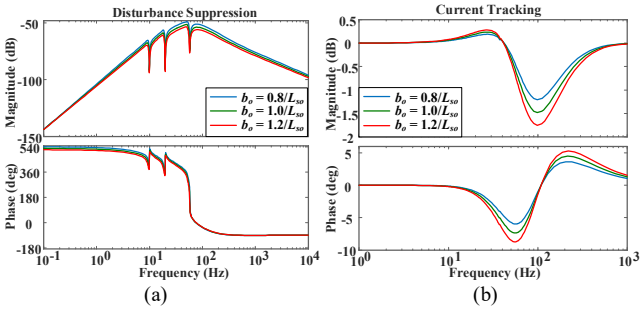

Fig. 10. The bode plots of $G_{\varepsilon i}(s)$ and $G_{ct}(s)$ of the FxTAESO-AFRC under different b_o variation. (a) $G_{\varepsilon i}(s)$; (b) $G_{ct}(s)$. (Parameter setting: $k_{r1} = 100$, $\omega_c = 0.002\pi$, $\xi = 1.5$, $k_{qp} = 100$, $\omega_0 = 200\pi$, $\omega_{h1} = 20\pi$, and $E_1 = 1$).

The corresponding Bode plot of the anti-noise transfer functions for both the proposed and conventional methods are illustrated in Fig. 9. As observed, the traditional observer exhibits minimal attenuation of noise amplitude below 10kHz, indicating its limited noise-suppression capability. In contrast, the proposed integral augmented strategy exhibits a gradual decay in noise magnitude, reaching approximately −100dB, thereby demonstrating its superior robustness against measurement noise. Specifically, at 1kHz and 3kHz, the proposed scheme achieves additional noise attenuation of 21.74dB and 32.61dB, respectively, compared with the conventional approach. Moreover, as the frequency increases, the proposed strategy exhibits progressively stronger noise suppression, confirming its remarkable anti-noise performance.

E. Parameters Robustness Analysis

During the long-term operation of PMSM system, the motor resistance and inductance will change with temperature and varying working conditions. And in the controller, b_o depends on the inductance parameter. The effect of other controller parameters on the performance such as disturbance suppression and current tracking has been discussed separately in the previous subsections. Therefore, it's necessary to analyze the effect of varying b_o over a certain range on the disturbance rejection capability and current tracking performance of the control system to verify the parameters robust characteristics of the designed scheme. Then, the robustness of the b_o at 0.8-1.2 times nominal value $1/L_{so}$ is explored for Eq. (40) and Eq. (41), respectively. The corresponding Bode plots are shown in Fig. 10.

It can be noticed that the value of b_o is proportional to the system disturbance suppression capability and inversely proportional to the current tracking performance. However, the system still maintains superior disturbance rejection and current tracking performance. The current can remain close to the tracking characteristics of unit gain and 0° phase. Therefore, the proposed FxTAESO-AFRC is proved to exhibit good parametric robustness.

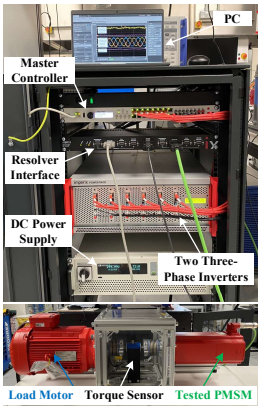

Fig. 11. Experimental motor test rigs.

TABLE I
BASIC PARAMETERS OF TESTED PMSM

Symbols	Variables	Values
p_n	Pole pairs	4
R_{so}	Stator resistance	0.559Ω
L_{so}	Stator inductance	4.24mH
ψ_{fo}	Flux of permanent magnet	0.2748Wb
U_{dc}	Bus voltage	300V
P_{ap}	Nominal active power	4.8kW
T_{emn}	Nominal torque	20Nm

F. Adaptive Function Design for $\xi = f(i_q, HRS, DPM)$

This section focuses on the design method of the adaptive function embedded within the proposed AFRC. As described in Eq. (31), the adaptive fractional-order exponential term ξ is jointly determined by the q-axis output current i_q, the harmonic rejection strength (HRS), and the desired phase margin (DPM) of the closed-loop system. Based on the harmonic analysis presented in Section II-B, it's evident that harmonic amplitude exhibits a direct correlation with the load magnitude I, which in turn, is proportional to the q-axis output current. Consequently, according to Eq. (40), the influence of current-induced harmonic disturbances on the system output current can be modeled as:

$$i_{q\varepsilon}(s)|_{s=j\omega} = \left[\frac{s}{s^2+Q(s)b_0}\cdot mi_q(s)\right]|_{s=j\omega} = A_H(\omega)e^{j\theta_H(\omega)} \quad (43)$$

where the positive proportional coefficient m quantifies the linear relationship between harmonic magnitude and the corresponding output current; $A_H(\omega)$ and $\theta_H(\omega)$ are the amplitude-phase-frequency characteristics of $i_{q\varepsilon}(s)$. To ensure adequate disturbance attenuation, a parameter denoted as HRS is introduced. This threshold defines the maximum permissible error current induced by harmonic disturbances. Therefore, it can be obtained that $A_H(\omega) < HRS$ needs to be satisfied at any frequency, and since the fractional-order exponential term ξ is negatively correlated with $A_H(\omega)$, the lower limit value ξ_{min} of the fractional-order exponential term ξ can be obtained according to the above inequality.

As inferred from Eq. (41), increasing the value of ξ enhances the suppression margin; however, this improvement comes at the cost of reduced system phase margin, potentially compromising closed-loop stability. Therefore, to strike a balance between rejection ability and stability, both the HRS and the DPM are employed to constrain the value of the adaptive fractional-order exponential term ξ. The closed-loop system transfer function can be deduced from Fig. 4 as:

$$G_{cl}(s)|_{s=j\omega} = \frac{Q(s)b_0 s}{s^2+Q(s)b_0}|_{s=j\omega} = A_C(\omega)e^{j\theta_C(\omega)} \quad (44)$$

where $A_C(\omega)$ and $\theta_C(\omega)$ are the amplitude-phase-frequency characteristics of $G_{cl}(s)$. Based on the condition $A_C(\omega_{cut}) = 1$, the cutoff frequency ω_{cut} of the closed-loop system can be analytically determined. To ensure adequate phase margin, the gain cutoff

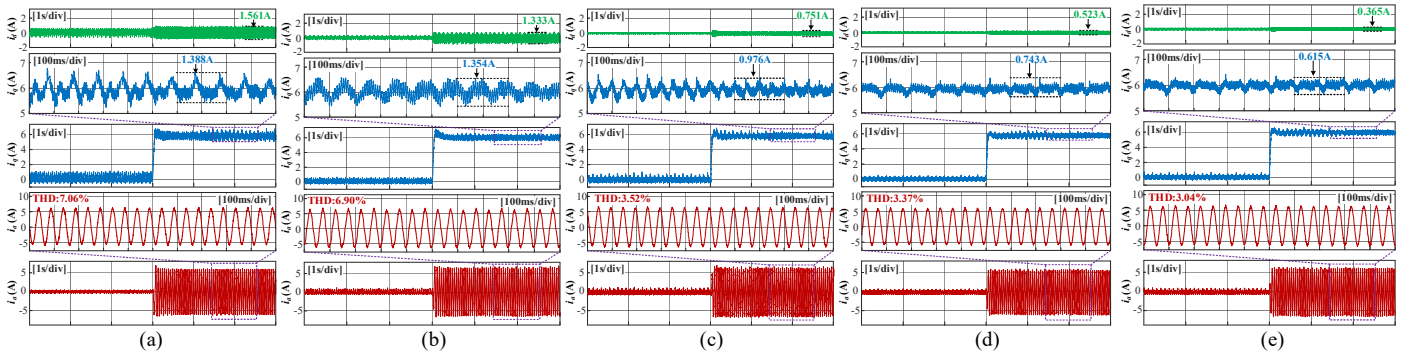

Fig. 12. The *d*-axis current, *q*-axis current, and A-phase current for five current control strategies under half rated load (10Nm). (a) PI, (b) TESO, (c) TESO-VRC, (d) FxTESO-AFRC, and (e) FxTAESO-AFRC.

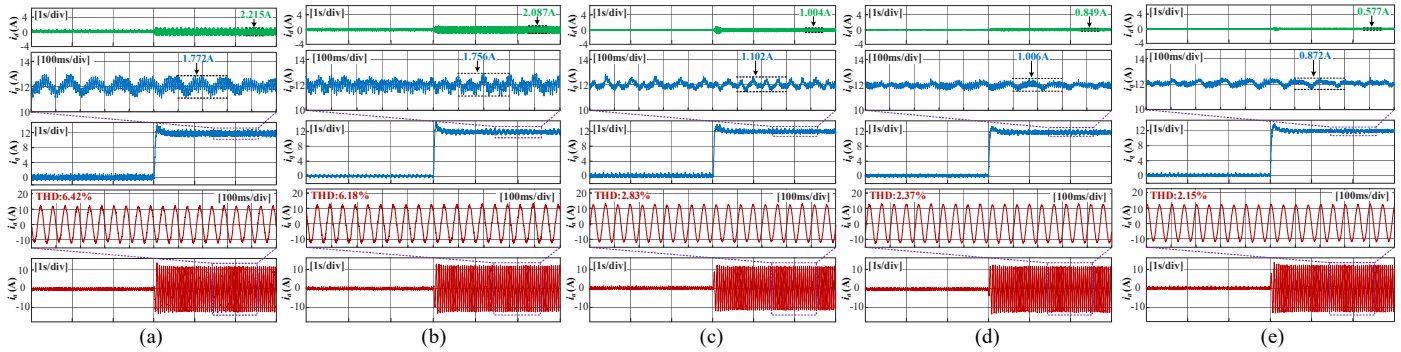

Fig. 13. The *d*-axis current, *q*-axis current, and A-phase current for five current control strategies under rated load (20Nm). (a) PI, (b) TESO, (c) TESO-VRC, (d) FxTESO-AFRC, and (e) FxTAESO-AFRC.

TABLE II
MAGNITUDES OF HARMONICS FOR Q-AXIS CURRENT (10NM/20NM)

Frequency	f_o(mA)	$2f_o$(mA)	$6f_o$(mA)
PI	246/258	218/231	217/251
TESO	233/244	153/178	148/202
TESO-VRC	147/179	73/102	101/119
FxTESO-AFRC	62/82	39/43	54/67
FxTAESO-AFRC	9.7/8.1	4.9/4.2	6.8/5.2

frequency must satisfy $\theta_C(\omega_{cut}) + 180° > DPM$. Furthermore, due to the inverse relationship between fractional-order exponential term ξ and $\theta_C(\omega) + 180°$, the upper limit value ξ_{max} of the fractional-order exponential term ξ can be accordingly derived.

Following this analytical framework, the adaptive fractional-order exponential term is ultimately selected as $\xi = (\xi_{max} + \xi_{min})/2$ to maintain sufficient phase margin and harmonic rejection margin. The determination of this adaptive fractional-order exponential term ξ involves a systematic three-step procedure. Firstly, the lower limit value ξ_{min} is established based on the load current and the HRS. Secondly, the upper limit value ξ_{max} is derived with respect to the DPM specifications. Finally, the adaptive rate is calibrated such that the exponent satisfies the condition $\xi = (\xi_{max} + \xi_{min})/2$. In the design of this paper, HRS and DPM are selected as 0.01 and 45°, respectively, and the *q*-axis output current ranges from 0 to the rated value 12A.

V. EXPERIMENTAL VERIFICATION

To fully validate the effectiveness of the proposed scheme, comparative experiments were conducted on the motor test rig shown in Fig. 11. Table I summarizes the nominal parameters of tested PMSM. The motors and controllers used in experiments are semi-physical test rigs from IMPERIX, Switzerland. It primarily comprises a master controller, a resolver interface, two three-phase inverters, a DC power supply, and dual motors. The tested PMSM is controlled by speed and current double-loop architecture. The speed loop is operated by a PI controller with the control period of $200\mu s$. And the parameters setting is $k_{p\_spd} = 1$ and $k_{i\_spd} = 15$. The current loop of tested PMSM is used to compare the performance of classical PI controller with optimal tunned parameters, traditional ESO [TESO, four-order nonlinear observer based on classical nonlinear correction term $fal(\rho, \alpha_i, e) = \begin{cases} \rho^{\alpha_i - 1} e, |e| \le \rho \\ |e|^{\alpha_i} sign(e), |e| > \rho \end{cases}$], TESO with vector resonant controller [TESO-VRC, VRC adopts the generalized form shown as $G_{VRC}(s) = \sum_{i=1,2,6} \frac{k_{ri}\omega_{ci} s(L_{so} s + R_{so})}{s^2 + \omega_{ci} s + \omega_{hi}^2}$], proposed AFRC with fixed-time extended state observer without the integral augmented variable (FxTESO-AFRC) and the proposed FxTAESO-AFRC. The corresponding parameters of the other comparative strategies remain identical to the proposed scheme. The load motor operates in a single torque loop with PI parameters $k_{p\_load} = 74$ and $k_{i\_load} = 4133$. In addition, the current control frequency is set to 20kHz for both motors and the deadtime intervals of inverters is selected as $1\,\mu s$ to balance the current harmonic content and equipment safety.

Since the proposed strategy introduces the measured current integral as a system augmentation variable, the decoupling of high observer gains and current measurement noise is directly realized. After practical experimental validation, it's found the proposed strategy can be set with a larger observer bandwidth without oscillation compared to TESO, thus achieving better current performance. However, to be fair, the same proportional gain and observer bandwidth are adopted for all above current control strategies in the following comparative experiments, as a way to highlight the proposed FxTAESO-AFRC still has optimal effects under the same parameters. Therefore, the proportional gain of control law and the observer bandwidth are set to $k_{pq} = k_{pd} = 1000$ and $\omega_0 = 200\pi$rad/s for all above control schemes. Furthermore, for the proposed strategy, the switching point ρ, variables α, and β are set to 0.001, 0.8, and 1.2, respectively. And the resonant gain and bandwidth satisfy $k_{ri} = ik_{r1}$, $\omega_{ci} = i\omega_{c1}$, $i = 1,2,6$ and $k_{r1} = 100, \omega_{c1} = 0.02\pi$rad/s. For FxTESO-AFRC strategy, all the parameters are identical with proposed scheme, the

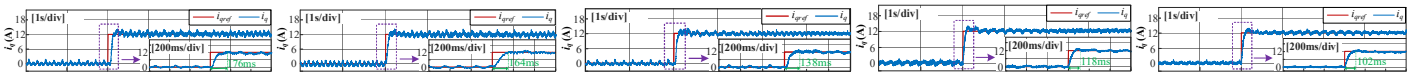

(a) (b) (c) (d) (e)

Fig. 14. Dynamic response of *q*-axis current under rated load step for five current control strategies. (a) PI, (b) TESO, (c) TESO-VRC, (d) FxTESO-AFRC, and (e) FxTAESO-AFRC.

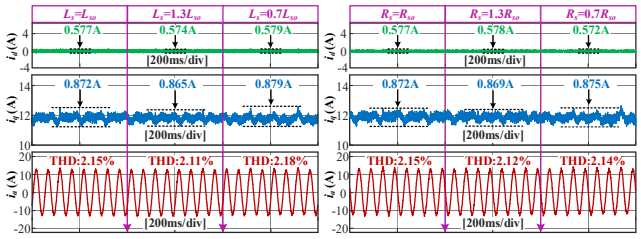

(a) (b)

Fig. 15. The *d*-axis current, *q*-axis current and A-phase current of proposed FxTAESO-AFRC under rated load with parameter variations. (a) Inductance variation, (b) resistance variation.

only difference is that FxTESO doesn't have the integral augmented variable. For TESO-VRC method, the design parameters of its VRC are kept the same as above. For classical PI controller, the optimal parameters $k_{p\_PI} = 14$ and $k_{i\_PI} = 1863$ are chosen to utilize the zero-pole elimination strategy. The running speed of tested PMSM is set to 300rpm.

A. Steady-State Performance Experiment

To validate steady-state performance of the proposed control strategy, multi-angle experimental verification of steady-state current fluctuations, output current total harmonic distortion (THD), and fast Fourier Transform (FFT) results of the five comparative strategies are hereby conducted under half rated load (10Nm) and rated load (20Nm). Under 10Nm load condition, it can be observed from Fig. 12(a) that the steady-state *dq*-axes currents ripples with PI scheme are 1.561A and 1.388A, respectively, and the A-phase current waveform has obvious aberrations, as well as the THD reaches as high as 7.06%. Furthermore, Table II shows the magnitudes of harmonics for *q*-axis current. It's obvious that the 1st, 2nd and 6th harmonics in the *q*-axis current dominate, which is highly consistent with the previous theoretical analysis. The amplitudes of these three harmonic contents have reached 246mA, 218mA and 217mA, respectively. And it can be seen from Fig. 12(b) that the steady-state *dq*-axes currents ripples with TESO scheme are 1.333A and 1.354A, respectively, and the A-phase current THD reaches as also high as 6.90%. The amplitudes of three harmonics are 233mA, 153mA and 148mA. Fig. 12(c) shows the experimental results with scheme TESO-VRC, from which *dq*-axes current, A-phase current THD, and three harmonic contents are attenuated to a certain extent due to the introduced VRC. The *dq*-axes current fluctuations and A-phase current THD are reduced to 0.751A, 0.976A, and 3.52%. The magnitudes of three harmonics are also attenuated to 147mA, 73mA, and 101mA. However, although current ripples and harmonic contents are decreased to some extent, the scheme doesn't achieve sufficient suppression, and the order of magnitudes of harmonics remain consistent with TESO. And it can be shown from Fig. 12(d) that the steady-state *dq*-axes currents ripples with FxTESO-AFRC scheme are 0.523A and 0.743A, respectively, and the A-phase current THD reaches 3.37%. The amplitudes of three harmonics are 62mA, 39mA and 54mA. Finally, Fig. 12(e) illustrates the experimental results plotted by adopting proposed FxTAESO-AFRC. The *dq*-axes steady-state current fluctuations and A-phase current THD have been substantially attenuated, with their values reduced to 0.365A, 0.615A, and 3.04%, respectively. The FFT analysis results of *q*-axis current can also be summarized that all three harmonics are adequately and completely suppressed, with the values of 9.7mA, 4.9mA, and 6.8mA, respectively. This also verifies the superiority of the proposed strategy under half rated load.

TABLE III
COMPUTATIONAL BURDEN OF SEVERAL COMPARISON SCHEMES

Scheme	PI	TESO	TESO-VRC	FxTESO-AFRC	FxTAESO-AFRC
Time	8.71μs	9.23μs	9.54μs	16.96μs	17.61μs

Fig. 13 shows the experimental results of five schemes under rated load. Fig. 13(a) demonstrates the *dq*-axes current ripples, A-phase current THD, and their values of 2.215A, 1.772A, and 6.42%, respectively, for taking the PI approach. The amplitudes of three harmonics are 258mA, 231mA, and 251mA. And Fig. 13(b) displays the *dq*-axes current ripples, A-phase current THD, and their values of 2.087A, 1.756A, and 6.18% for taking the TESO method. The amplitudes of three harmonics are 244mA, 178mA, and 202mA. Fig. 13(c) presents the results of adopting TESO-VRC strategy, which shows all the indexes have been attenuated to a certain extent, but there is still room for improvement. The *dq*-axes current ripples, A-phase current THD, and three harmonics are 1.004A, 1.102A, 2.83%, 179mA, 102mA, and 119mA. And Fig. 13(d) displays the *dq*-axes current ripples, A-phase current THD, and their values of 0.849A, 1.006A, and 2.37% for taking the FxTESO-AFRC method. The amplitudes of three harmonics are 82mA, 43mA, and 67mA. Fig. 13(e) illustrates the waveforms of proposed FxTAESO-AFRC, which displays both current ripples and three harmonics are maximally suppressed. The *d*-axis current fluctuation is reduced from 2.215A to 0.577A, with a reduction percentage of 73.95%. The *q*-axis current fluctuation is reduced from 1.772A to 0.872A, with a reduction percentage of 50.79%. And the A-phase current THD is reduced from 6.42% to 2.15%, with a reduction percentage of 66.51%. The amplitudes of three harmonics are decreased to the milliampere level with values of 8.1mA, 4.2mA, and 5.2mA, respectively. Thus, above experimental results fully validate the supremacy of proposed strategy in the case of steady-state.

B. Dynamic Performance Verification

Current dynamic characteristic is also an essential indicator of motor control performance. Fig. 14 illustrates the dynamic response of *q*-axis current of five comparative control strategies for a rated load step and localized magnification of the step transient. All the five strategies can realize accurate current tracking and fast response. However, due to the fixed-time convergence property of the proposed FxTAESO-AFRC method, its observation and compensation of disturbances and state variables respond faster under the same parameter constraints. Building upon this, it has the lowest response time with a value of 102ms, which is 42.05% faster compared to 176ms for PI, 37.80% faster compared to 164ms for TESO, 26.09% faster compared to 138ms for TESO-VRC and negligible difference compared to 118ms for FxTESO-AFRC. Furthermore, the proposed strategy achieves smoother and faster current dynamic since it has a much lower current fluctuation and transient overshoot.

C. Parameters Robustness

Because the PMSM parameters change in real-time with the working conditions and temperature during the actual operation. And in the controller design of this paper, it's known to be closely related to the inductance and resistance parameters according to Eq.

TABLE IV
COMPREHENSIVE PERFORMANCE COMPARISON OF FIVE SCHEMES

	Schemes	PI	TESO	TESO-VRC	FxTESO-AFRC	FxTAESO-AFRC
10Nm Load	D-axis Current Ripple (A)	1.561	1.333	0.751	0.523	0.365
	Q-axis Current Ripple (A)	1.388	1.354	0.976	0.743	0.615
	Phase-A Current THD (%)	7.06	6.90	3.52	3.37	3.04
	1st Order Harmonic (mA)	246	233	147	62	9.7
	2nd Order Harmonic (mA)	218	153	73	39	4.9
	6th Order Harmonic (mA)	217	148	101	54	6.8
20Nm Load	D-axis Current Ripple (A)	2.215	2.087	1.004	0.849	0.577
	Q-axis Current Ripple (A)	1.772	1.756	1.102	1.006	0.872
	Phase-A Current THD (%)	6.42	6.18	2.83	2.37	2.15
	1st Order Harmonic (mA)	258	244	179	82	8.1
	2nd Order Harmonic (mA)	231	178	102	43	4.2
	6th Order Harmonic (mA)	251	202	119	67	5.2
Dynamic Response (ms)		176	164	138	118	102
Computational Time (μs)		8.71	9.23	9.54	16.96	17.61

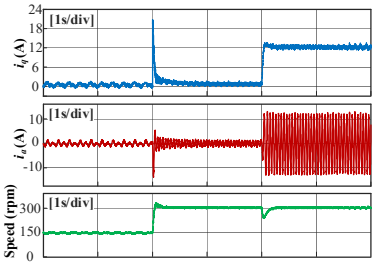

Fig. 16. The q-axis current, A-phase current and speed profiles of proposed FxTAESO-AFRC for 150rpm speed step and rated load step.

(33) and Eq. (34), so it's quite necessary to analyze the robustness of proposed scheme to these parameters. Fig. 15 displays dq-axis current and A-phase current waveforms of the motor inductance and resistance at nominal, 1.3 times nominal, and 0.7 times nominal parameters, respectively. The fluctuations of above currents and THD are nearly the same as the corresponding indexes under the nominal parameters, both in the case of inductance and resistance change. It's proved that the FxTAESO-AFRC is highly robust to parameter variations.

D. Comparison of Computational Burden

In an attempt to apply the algorithm to high-performance servo systems with fast control frequency, the computational burden of the processor for different schemes is extracted and displayed in Table III. The computational time of the four conventional schemes is $8.71\mu s$, $9.23\mu s$, $9.54\mu s$, and$16.96\mu s$, while the time of proposed strategy is $17.61\mu s$. This is because proposed FxTAESO-AFRC involves a nonlinear observer correction term and a fractional-order differential operator, which increases the processor's computational time to some extent. However, it's still much lower than the control period of $50\mu s$, and there still exists a large time margin to configure other parts of systems. The extra computational time is perfectly acceptable compared to current fluctuations and harmonics suppression performance. This also demonstrates its suitability for high control frequency.

In addition, to fully demonstrate where the differences in steady-state performance, dynamic response, and computation time lie between the five comparison strategies mentioned above. A comparative table regarding the improvement of the proposed control strategy is comprehensively exhibited as shown in Table IV. From the table, it can be seen that the proposed control strategy has optimal performance metrics in various scenarios.

E. Speed Dynamic Performance Test

The proposed FxTAESO-AFRC adopts a frequency adaptive principle to correct resonant frequencies in real-time according to the motor speed. Fig. 16 shows the results of speed dynamic performance tests conducted. The initial speed is set to 150rpm, and then a speed step of 150rpm is applied at 2s, and a rated load step is added at 4s. There are fluctuations in the q-axis current and A-phase current during the speed step and load step transients, but the current fluctuations quickly converge to lower values as the speed approaches its reference value. Thus, speed dynamic characteristic of proposed strategy is validated.

VI. CONCLUSION

The proposed strategy FxTAESO-AFRC can adaptively adjust resonant gain to balance harmonic rejection capability and system stability margin, and at the same time achieve noise immunity and observer's fast convergence by introducing current integral augmented variable and optimizing nonlinear correction term. Firstly, proposed AFRC incorporates an adaptive fractional-order operator term that varies adjustably in real-time with load current, harmonic rejection strength, and desired phase margin, thus adequately suppressing the periodic current disturbances while guaranteeing rejection ability and system stability. Subsequently, the proposed FxTAESO introduces a measured current integral term as the augmented variable to decouple interaction between current measurement noise and high observer gain. Additionally, the state estimation error can be driven to converge within the vicinity of the equilibrium point in a fixed time by proposing a reasonable nonlinear correction term. Finally, the practicalities and effectiveness of proposed scheme are experimentally verified on a PMSM platform. It's worth mentioning that the proposed strategy is also applicable to other types of motor systems such as permanent magnet linear synchronous motor (PMLSM), induction motor (IM), etc.

APPENDIX

Definition 1 [39]***:*** The vector field $\boldsymbol{f}(x)\colon \mathbb{R}^n \to \mathbb{R}^n$ is homogeneous of degree d with respect to weight $\boldsymbol{h}$, if for any $\boldsymbol{x} \in \mathbb{R}^n$ the relation $\boldsymbol{f}(\boldsymbol{\Lambda_h x}) = \lambda^d \boldsymbol{\Lambda_h f}(\boldsymbol{x})$ holds for some $d \geq -\min_{1\leq i\leq n} \boldsymbol{h}_i$ and all $\lambda > 0$. The function $V(x)\colon \mathbb{R}^n \to \mathbb{R}$ is homogeneous of degree d with respect to weight $\boldsymbol{h}$, if for any $\boldsymbol{x} \in \mathbb{R}^n$ the relation $V(\boldsymbol{\Lambda_h x}) = \lambda^d V(\boldsymbol{x})$ holds for some $d \in \mathbb{R}$ and all $\lambda > 0$. And if a vector field or function is homogeneous in both 0-limit and ∞-limit, then it will be considered to be homogeneous in the bi-limit.

Definition 2 [40]***:*** A vector field $\boldsymbol{f}(\mathbf{e})\colon \mathbb{R}^n \to \mathbb{R}^n$ (or a function $V(\mathbf{e})\colon \mathbb{R}^n \to \mathbb{R}$) is considered to be homogeneous in the q-limit ($q = 0$ or ∞) with corresponding triples $(\boldsymbol{h}_q, d_q, \boldsymbol{f}_q)$ (or $(\boldsymbol{h}_q, d_q, V_q)$) if the relationship

$$\begin{cases} \limsup\limits_{\substack{\lambda\to q \\ \mathbf{e}\in \boldsymbol{K}}} \left\| \lambda^{-d_q} \boldsymbol{\Lambda}_{\boldsymbol{h}_q}^{-1} \boldsymbol{f}\left(\boldsymbol{\Lambda}_{\boldsymbol{h}_q} \mathbf{e}\right) - \boldsymbol{f}_q(\mathbf{e}) \right\| = 0 \\ \limsup\limits_{\substack{\lambda\to q \\ \mathbf{e}\in \boldsymbol{K}}} \left\| \lambda^{-d_q} V\left(\boldsymbol{\Lambda}_{\boldsymbol{h}_q} \mathbf{e}\right) - V_q(\mathbf{e}) \right\| = 0 \end{cases}$$

for all compact subsets $\boldsymbol{K} \in \mathbb{R}^n\backslash\{0\}$, where $\boldsymbol{h}_q$ is the weight, $d_q \in \mathbb{R}$ is the degree, and $\boldsymbol{f}_q(\mathbf{e})\colon \mathbb{R}^n \to \mathbb{R}^n$ is the approximation vector field (or $V_q(\mathbf{e})\colon \mathbb{R}^n \to \mathbb{R}$ is the approximation function).

Lemma 1: For system (12), assuming that vector field $\boldsymbol{r}(\boldsymbol{e})$ is bi-limit homogeneous with vector triples $\left(\boldsymbol{h}_q, d_q, \boldsymbol{f}_q\right), q = 0$ or ∞. If the origins of system $\dot{\boldsymbol{e}} = \boldsymbol{r}(\boldsymbol{e})$ is globally asymptotically stable, then the following conclusions maintain: ***I.*** The origin of (12) is fixed-time stable when satisfies $d_\infty > 0 > d_0$. ***II.*** Make $d_{V_0} > \max_{1\le i\le n} \boldsymbol{h}_{0,i}, d_{V_\infty} > \max_{1\le i\le n} \boldsymbol{h}_{\infty,i}$ and d_{V_0}, d_{V_∞} be real numbers. There exists a continuous, positive definite and proper function $V(\boldsymbol{e})$ such that the function $\boldsymbol{e} \to \partial V/\partial e_i, \forall i \in \{1,2,\cdots,n\}$ is bi-limit homogeneous with vector triples $\left(\boldsymbol{h}_q, d_{V_q} - \boldsymbol{h}_{q,i}, \partial V_q/\partial e_i\right), q = 0\ or\ \infty$, and the functions $\boldsymbol{e} \to \partial V/\partial \boldsymbol{e} \cdot \boldsymbol{r}(\boldsymbol{e})$ and $\boldsymbol{e} \to \partial V_q/\partial \boldsymbol{e} \cdot \boldsymbol{r}_q(\boldsymbol{e})$ are negative definite.

Lemma 2: If $\mu(\mathbf{e})\colon \mathbb{R}^n \to \mathbb{R}$ and $\delta(\mathbf{e})\colon \mathbb{R}^n \to \mathbb{R}_+$ are two bi-limit homogeneous functions with triples $\left(\boldsymbol{h}_0, d_{\mu 0}, \mu_0\right)$, $\left(\boldsymbol{h}_\infty, d_{\mu\infty}, \mu_\infty\right)$, $(\boldsymbol{h}_0, d_{\delta 0}, \delta_0)$ and $\left(\boldsymbol{h}_\infty, d_{\delta\infty}, \delta_\infty\right)$, and satisfying $d_{\mu 0} \ge d_{\delta 0}, d_{\mu\infty} \le d_{\delta\infty}$ and $\delta, \delta_0, \delta_\infty$ are all positive definite, then there is a positive real number p holds $\mu(\mathbf{e}) \le p\delta(\mathbf{e}), \forall \mathbf{e} \in \mathbb{R}^n$.

REFERENCES

[1] C. Zhang et al., "An Adaptive ADRC Strategy With Weight Function for Propeller Speed Control and Experimental Verification in Wind Tunnel," *IEEE Trans. Transp. Electrif.*, vol. 10, no. 1, pp. 670-681, March 2024.

[2] X. Liu, H. Yang, H. Lin, F. Yu and Y. Yang, "A Novel Finite-Set Sliding-Mode Model-Free Predictive Current Control for PMSM Drives Without DC-Link Voltage Sensor," *IEEE Trans. Power Electron.*, vol. 39, no. 1, pp. 320-331, Jan. 2024.

[3] J. Ye, M. Wang, S. Cui, C. Zhang and L. Li, "Modified Single-Edge Modulation to Decrease Common-Mode Voltage with Considering Deadtime Effects and Switching Losses for Three-Phase VSIs," *IEEE Trans. Power Electron.*, vol. 39, no. 8, pp. 9292-9304, Aug. 2024.

[4] H. Cao, Y. Deng, Y. Zuo, H. Li, J. Wang and X. Liu, "Improved ADRC With a Cascade Extended State Observer Based on Quasi-Generalized Integrator for PMSM Current Disturbances Attenuation," *IEEE Trans. Transp. Electrif.*, vol. 10, no. 1, pp. 2145-2157, March 2024.

[5] Y. Yan, J. Yang, Z. Sun, C. Zhang, S. Li and H. Yu, "Robust Speed Regulation for PMSM Servo System With Multiple Sources of Disturbances via an Augmented Disturbance Observer," *IEEE/ASME Trans. Mechatron.*, vol. 23, no. 2, pp. 769-780, April 2018.

[6] Y. Yin, L. Liu, S. Vazquez, R. Xu, Z. Dong, J. Liu, J. Leon, L. Wu and L. Franquelo, "Disturbance and Uncertainty Attenuation for Speed Regulation of PMSM Servo System Using Adaptive Optimal Control Strategy," *IEEE Trans. Transp. Electrif.*, vol. 9, no. 2, pp. 3410-3420, June 2023.

[7] C. Mitsantisuk, K. Ohishi, and S. Katsura, "Estimation of action/reaction forces for the bilateral control using Kalman filter," *IEEE Trans. Ind. Electron.*, vol. 59, no. 11, pp. 4383–4393, Nov. 2012.

[8] F. Wang, K. Zuo, P. Tao, and J. Rodríguez, "High performance model predictive control for PMSM by using stator current mathematical model self-regulation technique," *IEEE Trans. Power Electron.*, vol. 35, no. 12, pp. 13652–13662, Dec. 2020.

[9] X. Zhang, B. Hou, and Y. Mei, "Deadbeat predictive current control of permanent-magnet synchronous motors with stator current and disturbance observer," *IEEE Trans. Power Electron.*, vol. 32, no. 5, pp. 3818–3834, May 2017.

[10] C. Zhang, C. Zhang, L. Li and H. Liu, "An Enhanced Nonlinear ADRC Speed Control Method for Electric Propulsion System: Modeling, Analysis, and Validation," *IEEE Trans. Power Electron*., vol. 38, no. 4, pp. 4520-4528, April 2023.

[11] M. Tian, B. Wang, Y. Yu, Q. Dong and D. Xu, "Enhanced One Degree-of Freedom ADRC With Sampled-Data Iterative Learning Controller for PMSM Uncertain Speed Fluctuations Suppression," *IEEE Trans. Transp. Electrif.*, vol. 10, no. 4, pp. 8321-8335, Dec. 2024.

[12] C. Tan, Q. Chen, L. Zhang and K. Zhou, "Frequency-Adaptive Repetitive Control for Three-Phase Four-Leg V2G Inverters," *IEEE Trans. Transp. Electrif.*, vol. 7, no. 4, pp. 2095-2103, Dec. 2021.

[13] C. Xia, B. Ji, and Y. Yan, "Smooth speed control for low-speed high-torque permanent-magnet synchronous motor using proportional integral-resonant controller," *IEEE Trans. Ind. Electron*., vol. 62, no. 4, pp. 2123–2134, Apr. 2015.

[14] B. Guo, S. Bacha, M. Alamir, A. Hably, and C. Boudinet, "Generalized integrator-extended state observer with applications to grid-connected converters in the presence of disturbances," *IEEE Trans. Control Syst. Technol.,* vol. 29, no. 2, pp. 744-755, Mar. 2021.

[15] Y. Zuo et al., "Active disturbance rejection controller for smooth speed control of electric drives using adaptive generalized integrator extended state observer," *IEEE Trans. Power Electron.,* vol. 38, no. 4, pp. 4323-4334, April 2023.

[16] A. G. Yepes, F. D. Freijedo, Ó. Lopez, and J. Doval-Gandoy, "High performance digital resonant controllers implemented with two integrators," *IEEE Trans. Power Electron*., vol. 26, no. 2, pp. 563–576, Feb. 2011.

[17] K. Rsetam, Z. Cao and Z. Man, "Cascaded-Extended-State-Observer-Based Sliding-Mode Control for Underactuated Flexible Joint Robot," *IEEE Trans. Ind. Electron*., vol. 67, no. 12, pp. 10822-10832, Dec. 2020.

[18] K. Rsetam, Z. Cao and Z. Man, "Design of Robust Terminal Sliding Mode Control for Underactuated Flexible Joint Robot," *IEEE Trans. Syst. Man Cybern.: Syst.*, vol. 52, no. 7, pp. 4272-4285, July 2022.

[19] Rsetam, Kamal, Zhenwei Cao, Lulu Wang, Mohammad Al-Rawi, and Zhihong Man. "Practically Robust Fixed-Time Convergent Sliding Mode Control for Underactuated Aerial Flexible Joint Robots Manipulators" *Drones*, vol. 6, no. 12: 428, 2022.

[20] Khan, R.F.A., Rsetam, K., Cao, Z. *et al.* "ESO Based Adaptive Fixed-Time Integral Sliding Mode Control for Flexible Joint Robots Using Singular Perturbation Method," *Nonlinear Dyn*, 113, 24981–25000, 2025.

[21] H. Cao et al., "Improved Deadbeat Predictive Current Control of PMSM Drives With Repetitive Control-Based Disturbance Correction Observer," *IEEE Trans. Power Electron.*, vol. 40, no. 1, pp. 801-812, Jan. 2025.

[22] Z. Sun, Y. Deng, J. Wang, T. Yang, Z. Wei and H. Cao, "Finite Control Set Model-Free Predictive Current Control of PMSM With Two Voltage Vectors Based on Ultralocal Model," *IEEE Trans. Power Electron.*, vol. 38, no. 1, pp. 776-788, Jan. 2023.

[23] H. Cao, Y. Deng, Y. Zuo, X. Liu, J. Wang and C. H. T. Lee, "A Variable Structure ADRC for Enhanced Disturbance Rejection and Improved Noise Suppression of PMSM Speed System," *IEEE Trans. Ind. Electron.*, vol. 72, no. 5, pp. 4481-4495, May 2025.

[24] Q. Hou, S. Ding and X. Yu, "Composite Super-Twisting Sliding Mode Control Design for PMSM Speed Regulation Problem Based on a Novel Disturbance Observer," *IEEE Trans. Energy Convers*., vol. 36, no. 4, pp. 2591-2599, Dec. 2021.

[25] J. Ye, M. Wang, S. Cai, C. Zhang and L. Li, "Fractional-Order Phase-Corrected Feedforward Repetitive Control With Fast Convergent Augmented Observer for Static-Errorless Current Regulation in PMSM," *IEEE Trans. Ind. Electron.*, early access, doi: 10.1109/TIE.2025.3605462.

[26] Q. Chen, X. Yu, M. Sun, C. Wu and Z. Fu, "Adaptive Repetitive Learning Control of PMSM Servo Systems with Bounded Nonparametric Uncertainties: Theory and Experiments," *IEEE Trans. Ind. Electron.*, vol. 68, no. 9, pp. 8626-8635, Sept. 2021.

[27] F. Song, Y. Liu, D. Shen, L. Li and J. Tan, "Learning Control for Motion Coordination in Wafer Scanners: Toward Gain Adaptation," *IEEE Trans. Ind. Electron.*, vol. 69, no. 12, pp. 13428-13438, Dec. 2022.

[28] J. Li, M. Wang, C. Zhang, M. Liu and L. Li, "High-Performance Control Method for Six-Degree-of-Freedom Micromotion Stage Based on High-Order Sliding Mode Control Theory," *IEEE Trans. Power Electron.*, vol. 39, no. 8, pp. 9174-9188, Aug. 2024.

[29] S. Jia, D. Yang, P. Sun, D. Liang and J. Si, "Decoupled Current Control Using Adaptive Quasi Resonant-Based ESO for Novel Matrix-Torque-Component Machines," *IEEE Trans. Power Electron.*, vol. 40, no. 6, pp. 8503-8515, June 2025.

[30] C. Du, S. Yang, L. Qiu, J. Ma, Y. Fang and J. Rodriguez, "A Cross-Decoupled Current Harmonics Suppression Method for IPMSM Based on Notch Filter and Second-Order Generalized Integrator," *IEEE Trans. Power Electron.*, vol. 40, no. 4, pp. 5715-5730, April 2025.

[31] M. Hu, W. Hua, G. Ma, S. Xu and W. Zeng, "Improved Current Dynamics of Proportional-Integral-Resonant Controller for a Dual Three-Phase FSPM Machine," *IEEE Trans. Ind. Electron.*, vol. 68, no. 12, pp. 11719-11730, Dec. 2021.

[32] J. Han, "From PID to Active Disturbance Rejection Control," *IEEE Trans. Ind. Electron.*, vol. 56, no. 3, pp. 900-906, March 2009.

[33] K. Rsetam, Z. Cao, Z. Man and X. -M. Zhang, "GPIO-Based Continuous Sliding Mode Control for Networked Control Systems Under Communication Delays with Experiments on Servo Motors," *IEEE-CAA J. Automatica Sin*., vol. 12, no. 1, pp. 99-113, January 2025.

[34] W. Perruquetti, T. Floquet, and E. Moulay, "Finite-time observers: Application to secure communication," *IEEE Trans. Autom. Control*, vol. 53, no. 1, pp. 356–360, Feb. 2008.

[35] E. Bernuau, D. Efimov, W. Perruquetti, and A. Polyakov, "On homogeneity and its application in sliding mode control," *J. Franklin Inst*., vol. 351, pp. 1866–1901, Apr. 2014.

[36]A. Oustaloup, F. Levron, B. Mathieu and F. M. Nanot, "Frequency-band complex noninteger differentiator: characterization and synthesis," *IEEE Trans. Circuits Syst. I: Fundam. Theory Appl.*, vol. 47, no. 1, pp. 25-39, Jan. 2000.
[37]R. Xu, X. Shen, X. Lin, Z. Liu, D. Xu and J. Liu, "Robust Model Predictive Control of Position Sensorless-Driven IPMSM Based on Cascaded EKF-LESO," *IEEE Trans. Transp. Electrif.*, vol. 11, no. 4, pp. 8824-8832, Aug. 2025.
[38]Z. Wang, J. Zhao, L. Wang, M. Li and Y. Hu, "Combined Vector Resonant and Active Disturbance Rejection Control for PMSLM Current Harmonic Suppression," *IEEE Trans. Ind. Informat.*, vol. 16, no. 9, pp. 5691-5702, Sept. 2020.
[39]M. Basin, P. Yu, and Y. Shtessel, "Finite- and fixed-time differentiators utilising HOSM techniques," *IET Control Theory Appl.*, vol. 11, no. 8, pp. 1144–1152, 2017.
[40]T. Menard, E. Moulay, and W. Perruquetti, "Fixed-time observer with simple gains for uncertain systems," *Automatica*, vol. 81, pp. 438-446, Jul. 2017.